# A Novel Intercalibration Method for Fengyun(FY)-3 VIRR Using MERSI Onboard the Same Satellite Based on Pseudo-Invariant Pixels

Junwei Wang, Xiuqing Hu, *Member, IEEE*, Kun Gao, *Member, IEEE*, Yuqing He, Ling Wang, Guorong Li, Na Xu, and Peng Zhang, *Senior Member, IEEE*

*Abstract*—This study presents a novel approach to the radiometric intercalibration between two sensors onboard the same satellite based on pseudo-invariant pixels (PIPs) using iteratively reweighted multivariate alteration detection (IR-MAD) method. The IR-MAD algorithm can statistically select PIPs from the multispectral image pair to assess the radiometric differences between them. Analysis of multiple image pairs from different acquisition times can provide long-term intercalibration results for the two sensors. The procedure is applied to Fengyun(FY)-3A&3B visible infrared radiometer (VIRR), with the medium resolution spectral imager (MERSI) onboard the same platform as the reference. Consistency of the spatial distribution of the PIPs selected by IR-MAD with pseudo-invariant calibration sites (PICSs) given by other scientists demonstrates the effectiveness of our method. The long-term time series trending of top-of-atmosphere (TOA) VIRR reflectance over LIBYA1 and LIBYA4 after intercalibration correction shows that the intercalibrated VIRR has good agreement with MERSI, with a mean bias of less than 1% and an uncertainty of less than 2% for most channels. The approach requires no prior knowledge of the intercalibration targets and extends PICS to the pixel-level targets, which results in more diverse samples, broader dynamic ranges, and lower uncertainty, yielding consistent and reliable long-term intercalibration results.

*Index Terms*—Intercalibration, iteratively reweighted multivariate alteration detection (IR-MAD), medium resolution spectral imager (MERSI), pseudo-invariant pixels (PIPs), visible infrared radiometer (VIRR).

## I. INTRODUCTION

**Q**UANTITATIVE remote sensing depends on the Earth-observing (EO) sensors to provide reliable, accurate, and consistent measurements over time, especially for the long-term trend monitoring of the Earth system. In order to benefit fully from the ever-increasing number of EO satellite systems, intercalibration between the sensors is critical to bring the measurements from various imaging sensor systems to a common radiometric scale and hence sensor radiometric calibration is of critical importance [1].

The intercalibration is a technique to use a well-calibrated sensor as a reference to intercalibrate other sensors with near-simultaneous observations of the common targets on the surface of the Earth, Moon, or mutual reference to pseudo-invariant features [2]. Consistency biases between different sensors can be introduced from temporal, geometric, and spatial variation in sampling, as well as relative spectral response (RSR) differences and sensor degradation after launch. Regular intercalibration is necessary for data continuity and consistency from different imaging sensors, particularly for those without onboard calibrators or where vicarious calibrations are limited. A number of studies have shown that intercalibration is one of the potential techniques for long-term radiometric trending and quantifying radiometric bias for relative and absolute calibration [3], [4], [5], [6], [7], [8].

Numerous approaches to intercalibration between the sensors have been developed and implemented to better quantify the radiometric biases, and new methodologies continue to evolve. They mainly differ in degrees of simultaneity between sensors and the associated ancillary data. The vicarious ground-based calibration method, such as radiance- or reflectance-based methods, rely on simultaneous surface measurements and radiative transfer code computations [1], [9], [10], [11], [12], [13], [14]. However, these methods typically involve field campaigns, which are cost and labor intensive, hence the number of such calibrations is limited. In an attempt to have more frequent calibration or validation opportunities, certain targets have been used to calibrate or intercalibrate satellite sensors, including pseudo-invariant calibration sites (PICSs) [15], [16], [17], deep convective cloud (DCC) [17], [18], sunglint [19], [20], and the Moon [21], [22]. The simultaneous nadir overpass (SNO) method [3], [7], [23], [24] was proposed to assess the radiometric consistency between two satellites at the orbital intersections to further reduce uncertainties due to such effects as bidirectional reflectance distribution factor (BRDF). The SNO method was later extended to low latitude (SNO-*x*) [8], which makes comparisons over deserts and green vegetation possible. These methods generally depend on a series of elaborate thresholds

of simultaneity applied to collocate the data of sensors to minimize the consistency biases that may be attributed to BRDF effects or different contributions of the target spectral signature and atmosphere composition to the spectral response functions (SRFs), and therefore still constrain the opportunities for high quality and frequent sensor calibration and evaluation.

The motivation behind this study is the potential opportunity for an accurate and highly frequent long-term intercalibration for satellite sensors. An iteratively reweighted multivariate alteration detection (IR-MAD) based method is proposed to automatically select pseudo-invariant pixels (PIPs) in the scene for intercalibration. The PIPs selected by our method are pixel-level, which do not depend on large spatially homogeneous areas, such as PICS. Moreover, the IR-MAD-based method can select a greater number of samples with a wider variety of surface types than those selected by the SNO or SNO-*x* method, resulting in a wider dynamic range of reflectance for intercalibration. The approach requires no prior knowledge of the intercalibration targets and provides intercalibration results with high frequency. We describe the method and its implementation on the interclibration of the visible near-infrared (VNIR) bands of visible infrared radiometer (VIRR) onboard Fengyun(FY)-3A&B satellites with medium resolution spectral imager (MERSI) onboard the same platform. Note that this method is also applicable to other situations where the sensors for intercalibration are onboard different platforms, such as SNO or SNO-*x* events. Results of intercalibration between VIRR and MERSI on the same platform demonstrate the efficacy of our method.

## II. Sensor Overview and Data

### A. Sensor Description

*1) FY-3/VIRR:* A VIRR is a multiband imager which inherited from FY-1C and FY-1D and continued to be carried onboard FY-3 series sun-synchronous satellites. The involved satellites in this study, i.e., FY-3A and FY-3B, are a morning satellite with equator crossing time (ECT) at 10:00 and an afternoon satellite with ECT at 13:30, respectively. VIRR has ten channels, of which seven VNIR channels and three thermal infrared (TIR) channels, with a spatial resolution of 1.1 km at nadir for all bands. More details and channel specifications are illustrated in [25]. VIRR is not equipped with an onboard calibration system for reflective solar bands (RSBs). The in-orbit test and postlaunch vicarious calibration found that the prelaunch calibration coefficients for the VIRR solar bands are not applicable [26]. The operational calibration depends on the annual site calibration campaign in Dunhuang. However, the operational calibration coefficients are not updated annually, thus the accurate and frequent calibration for the VIRR RSBs is necessary.

*2) FY-3/MERSI:* MERSI is the keystone payload, which is a completely new generation imager of FY-3 series satellites. MERSI has 20 spectral bands, of which 19 are RSBs and one is a TIR band, covering the visible, near-infrared, and TIR spectra. MERSI scans the Earth through a 45° scan mirror in concordance with one *K*-mirror (derotation), resulting in a swath of 2900 km cross-track by 10 km along the track

(at nadir) for each scan [27]. The spatial resolution at the nadir of bands 1–5 is 250 m, whereas 1000 m for the remaining 15 bands. See [25] for more details and channel specification of MERSI. The MERSI is equipped with a visible onboard calibrator (VOC), which is a 6-cm-diameter integrating minisphere designed to monitor the system radiometric response changes that arise either from the MERSI degradation or a change in the output of VOC. However, due to the significant degradation of VOC itself, it is not used for updating calibration coefficients on orbit [27]. In practice, the operational calibration coefficients of MERSI are updated based on the vicarious calibration using the global multisites method and field measurement campaigns conducted in China radiometric calibration sites, i.e., Dunhuang. Many vicarious calibration methods have been conducted to MERSI and the overall uncertainty in the MERSI top-of-atmosphere (TOA) radiance or reflectance is less than 5% [27]. In this study, the long-term degradation of MERSI is monitored and corrected using the method in [28], and the results align consistently with other vicarious calibration methods.

### B. Study Area and Data

The region of interest (ROI) for this study is located in North Africa, as shown in Fig. 1. The reasons for selecting this region as ROI are as follows: 1) this region is mainly made up of desert with almost no vegetation because a high reflectance can reduce uncertainties from the atmospheric path radiance due to higher signal-to-noise ratio; 2) this region is arid to minimize the influence of atmospheric water vapor and has minimal cloud cover and precipitation; 3) this region is relatively spatial uniform to minimize the effects of misregistration in intercalibration; 4) the surface of this region is relatively spectrally uniform, which is particularly important for the matching spectral bands that have different spectral response profiles in intercalibration; and 5) several reference PICSs in this region, such as LIBYA1 and LIBYA4, can be used to evaluate the intercalibration accuracy.

In this study, the L1B level data of MERSI and VIRR are used for intercalibration. Experiments were carried out on FY-3A and FY-3B, respectively, to demonstrate the efficacy and generality of the proposed method. The range of the data covers almost the entire life cycle of the satellite, as illustrated in Table I.

## III. Methodology

### A. Intercalibration Formulation

Although the aperture spectral radiance is actually measured by the sensor, three advantages of converting the at-sensor spectral radiance to TOA reflectance were reported in [29]. Using TOA reflectances instead of radiance can reduce image-to-image variability and is a fundamental step in bringing image data from multiple sensors and platforms to a common scale. For a Lambertian surface in spectral band $i$, the TOA reflectance can be computed as follows:

$$\rho_i = \frac{\pi d^2 L_i}{E_{0i} \cos \theta} = \frac{\pi}{E_{0i}} \frac{d^2}{\cos \theta} (\mathrm{DN}_i - C_{0i}) S_i \qquad (1)$$
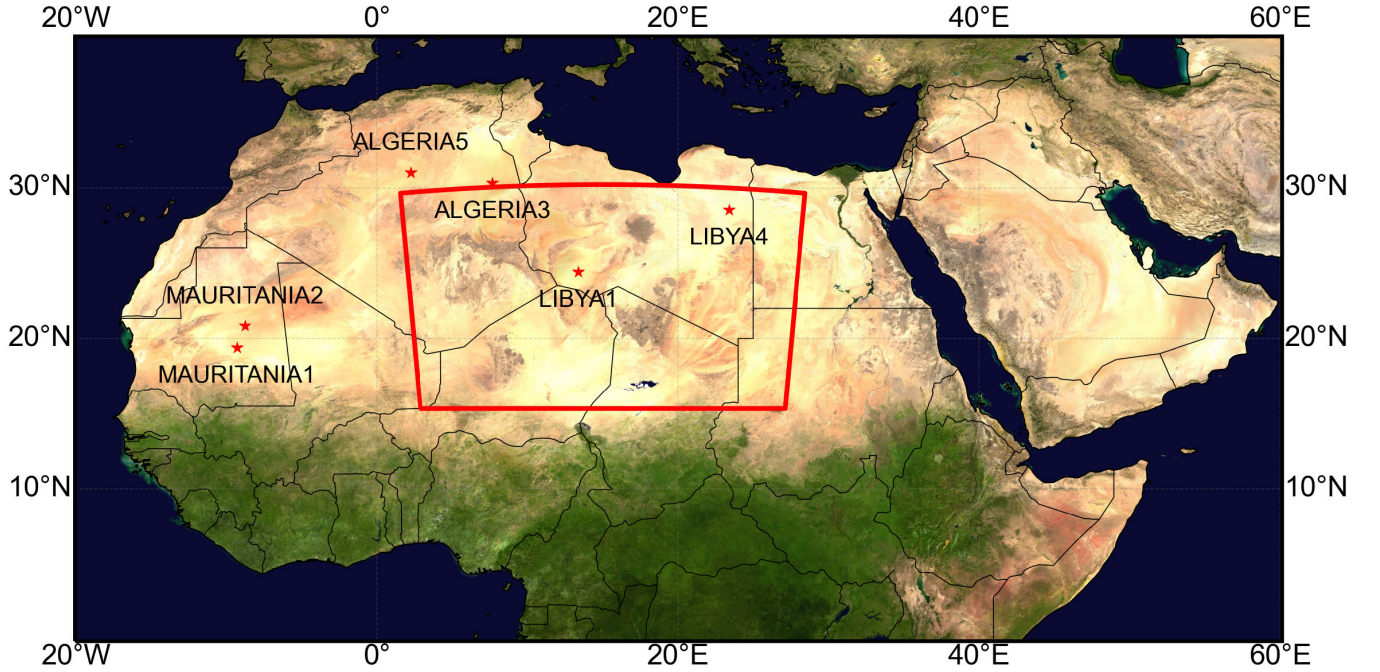
Fig. 1. ROI in this study. The six reference PICS defined by CEOS are marked as stars, of which LIBYA1 and LIBYA4 are located within the ROI.

TABLE I
TIME RANGE OF FY-3A AND FY-3B DATA USED IN THIS STUDY

|  | Start date | End date | Time span |
| --- | --- | --- | --- |
| FY-3A | Nov. 12, 2008 | Dec. 31, 2014 | >6 years |
| FY-3B | Jan. 21, 2011 | Nov. 14, 2018 | ≈8 years |

where $L_i$ is the spectral radiance at the sensor's aperture [in W/(m$^2$ sr $\mu$m)], $E_{0i}$ is the mean exo-atmospheric solar irradiance [in W/(m$^2$ $\mu$m)] that can be obtained by convolving the solar spectra [30] with the SRF of a given instrument. $d$ is the Earth–Sun distance in astronomical units (AUs), and $\theta$ is the solar zenith angle. DN$_i$ represents a raw digital number (in counts) recorded at the satellite, $C_{0i}$ is the zero-radiance response (in counts), and $S_i$ is the sensor sensitivity coefficient in units of percent reflectance per unit count.

In this study, MERSI is used as the reference sensor to intercalibrate VIRR onboard the same platform. Suppose MERSI is well-calibrated, the consistency bias between the two sensors comes from their SRF differences, calibration differences, and the VIRR degradation after launch. In this context, the (1) can be expressed separately for image data from the MERSI ("M") and for image data from the VIRR ("V") as follows:

$$\rho_{Mi} = \frac{\pi d^2 L_{Mi}}{E_{0Mi} \cos\theta} = \frac{\pi}{E_{0Mi}} \frac{d^2}{\cos\theta}(\text{DN}_{Mi} - C_{0Mi})S_{Mi} \quad (2)$$

$$\rho_{Vi} = \frac{\pi d^2 L_{Vi}}{E_{0Vi} \cos\theta} = \frac{\pi}{E_{0Vi}} \frac{d^2}{\cos\theta}(\text{DN}_{Vi} - C_{0Vi})S_{Vi} \quad (3)$$

where $i$ is the spectrally matching band of MERSI and VIRR. In practice, a fixed sensitivity coefficient from the early operational stage is adopted to calculate the nominal TOA reflectance. Accordingly, (2) and (3) can be rewritten as

$$\rho_{Mi}^* = \frac{\pi}{E_{M0}} \frac{d^2}{\cos\theta}(\text{DN}_{Mi} - C_{0Mi})S_{Mi0}$$

$$= \frac{\pi}{E_{M0}} \frac{d^2}{\cos\theta}(\text{DN}_{Mi} \cdot \alpha_{Mi} + \beta_{Mi}) \quad (4)$$

$$\rho_{Vi}^* = \frac{\pi}{E_{V0}} \frac{d^2}{\cos\theta}(\text{DN}_{Vi} - C_{0Vi})S_{Vi0}$$

$$= \frac{\pi}{E_{V0}} \frac{d^2}{\cos\theta}(\text{DN}_{Vi} \cdot \alpha_{Vi} + \beta_{Vi}) \quad (5)$$

where $\rho_{Mi}^*$ and $\rho_{Vi}^*$ are nominal TOA reflectance calculated by the fixed sensitivity coefficients $S_{Mi0}$ and $S_{Vi0}$. Since VIRR has degradation over time, it is useful to further separate the sensitivity coefficient into a fixed initial component and a time-varying component as

$$S_{Vi} = S_{Vi0} \cdot S_{Vi}(t) \quad (6)$$

where $t$ represents days since the first day ($S_{Vi0}$). $S_{Vi}(t)$ is the inverse of the relative degradation. Note that the MERSI is supposed to be well-calibrated, therefore,

$$S_{Mi} = S_{Mi0} \cdot S_{Mi}(t), S_{Mi}(t) = 1 \rightarrow S_{Mi} = S_{Mi0}. \quad (7)$$

The TOA reflectance of MERSI can be compensated with the spectral band adjustment factor (SBAF) $f_{\text{SBAF}}$ and the relative calibration factor $f_0$, where $f_{\text{SBAF}}$ accounts for SRF differences and $f_0$ explains calibration differences for the fixed sensitivity coefficients adopted in (4) and (5). Then,

$$\rho_{Vi} = f_0 \cdot f_{\text{SBAF}} \cdot \rho_{Mi}. \quad (8)$$

The combination of (2) to (8) yields

$$\rho_{Vi}^* = \frac{f_0 \cdot f_{\text{SBAF}}}{S_{Vi}(t)} \rho_{Mi}^*. \quad (9)$$

In practice, the $\alpha_i$ and $\beta_i$ can be read directly from the first day L1B file for MERSI and VIRR. The $f_0$ we want to obtain is contained in the slope of the linear equation that characterizes $\rho_{Vi}^*$ as a function of $\rho_{Mi}^*$. Once we get the degradation rate
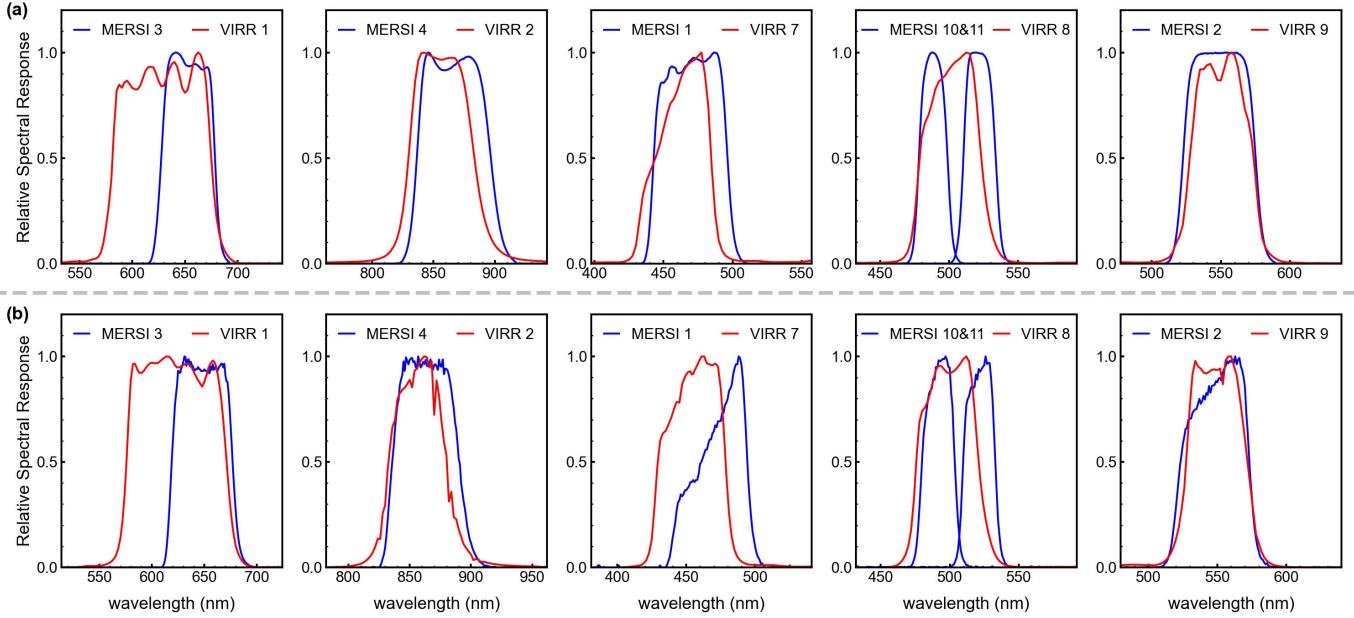
Fig. 2. Relative SRFs of matching channels between VIRR and MERSI for (a) FY-3A and (b) FY-3B.

function $S_{Vi}(t)$ and relative calibration factor $f_0$, the updated value of VIRR sensitivity coefficients is then given by

$$S_{Vi} = \frac{S_{Vi0} \cdot S_{Vi}(t)}{f_0} = \frac{\alpha_{Vi} \cdot S_{Vi}(t)}{f_0}. \tag{10}$$

With this updated value of $S_{Vi}$, users can obtain TOA reflectance of VIRR from (3).

### B. Spectral Band Matching

Different sensors have varying channels and spectral coverage ranges. Even if two sensors have similar spectral ranges in a given channel, differences in their RSRs may still exist. Fig. 2 displays the SRFs of matching channels between VIRR and MERSI. The differences in RSRs can lead to systematic biases in measurements of the same radiation source. Therefore, in intercalibration, the differences caused by the RSRs differences between the two sensors need to be addressed. This can be compensated for by using the SBAF. The definition and calculation of SBAF are documented in [31].

In this study, the scanning imaging absorption spectrometer for atmospheric chartography (SCIAMACHY) hyperspectral data was used to calculate the SBAF for each matching channel between VIRR and MERSI. The SRF was convolved with the hyperspectral data, and the SBAF values were obtained by performing linear regression on all samples. A total of 44 511 spectral samples were used, representing one full year of SCIAMACHY data within the ROI and encompassing the spectra of all surface types within the ROI. For VIRR channel 8, a binary linear regression was performed since it matches with two MERSI channels. The SBAF values, center wavelength (CW), correlation coefficient ($r$), and residual standard deviations for each matching channel between VIRR and MERSI are presented in Table II. Note that there may

TABLE II
MATCHING CHANNELS BETWEEN VIRR AND MERSI ON FY-3A AND FY-3B, TOGETHER WITH THE SBAF AND REGRESSION RESULTS CALCULATED BY USING SCIAMACHY DATA

| satellite | VIRR | | MERSI | | SBAF | r | residual std(%) |
|---|---|---|---|---|---|---|---|
| | band | CW | band | CW | | | |
| FY3A | 1 | 0.630 | 3 | 0.650 | 0.9557 | 0.9973 | 1.31 |
| | 2 | 0.865 | 4 | 0.865 | 0.9867 | 0.9998 | 0.32 |
| | 7 | 0.455 | 1 | 0.470 | 0.9939 | 0.9999 | 0.51 |
| | 8 | 0.505 | 10 | 0.490 | 0.6371 | 0.9999 | 0.36 |
| | | | 11 | 0.520 | 0.3681 | | |
| | 9 | 0.555 | 2 | 0.550 | 1.015 | 0.9990 | 1.15 |
| FY3B | 1 | 0.630 | 3 | 0.650 | 0.9650 | 0.9969 | 1.44 |
| | 2 | 0.865 | 4 | 0.865 | 0.9921 | 0.9998 | 0.33 |
| | 7 | 0.455 | 1 | 0.470 | 0.9863 | 0.9995 | 0.94 |
| | 8 | 0.505 | 10 | 0.490 | 0.6846 | 1.0000 | 0.15 |
| | | | 11 | 0.520 | 0.3114 | | |
| | 9 | 0.555 | 2 | 0.550 | 0.9993 | 1.0000 | 0.02 |

also be cloudy spectral samples. Examination of the regression plot reveals that there are no outliers, which can be verified by the residual standard deviations in Table I. The slightly higher residual standard deviation of VIRR band 1 is primarily attributed to the substantial difference in spectral bandwidth between VIRR band 1 and MERSI band 3 as shown in Fig. 2. As stated in [31], narrow-band RSRs are more sensitive to changes in the spectrum, leading to a more pronounced effect on SBAF compared to the wideband sensor RSR. The matched bands of VIRR and MERSI, they are all broad bands with bandwidth greater than 50 nm and have weakly gaseous absorption, resulting in the SBAF being less sensitive to the spectral variability of the samples. Hence the impact of cloudy samples on the SBAF regression is negligible.

### C. IR-MAD Method for Intercalibration

The multivariate alteration detection (MAD) technique was first proposed for change detection by Nielsen et al. [32].

This technique has been used in the automatic normalization of remote sensing images [33], and also for the radiometric calibration of AVHRR reflective bands [34]. An iteratively reweighted modification of the MAD transformation (IR-MAD) has been introduced [35] and was extended to radiometric normalization with substantial improvement [36]. This method was later applied to the selection of PICSs in Northwest China [37]. In this study, the IR-MAD technique is used to statistically select pixel-level targets for intercalibration. Next, the basic principles of IR-MAD and how it is applied to intercalibration are explained.

The MAD method can be used to automatically select invariant pixels for multispectral satellite imagery. In the context of radiometric normalization, the invariant pixels for bitemporal image refer to those that are temporally invariant across all spectral bands data during the acquisition time interval. The MAD transformation is linear scale-invariant under affine transformations of either or both of the original multispectral images, which is explicitly demonstrated in [33]. For intercalibration, as shown in (9), there is a linear relationship between the nominal TOA reflectance of the two sensors in matching bands. Given the invariance property of the MAD transformation, it is reasonable to use the MAD algorithm to select PIPs that are suitable for intercalibration. Instead of temporally invariant pixels, the PIPs here refer to the pixels that have linear scale invariance under two sensors with different spectral response characteristics in matching bands. Specifically, the PIPs represent the pixels that conform to the linear relationship in all matching bands under the differences caused by a combination of the RSR characteristics of the two sensors, the spectral signature of the target, and the atmospheric composition during the overpass. It is intuitively conceivable that when the SRF difference between the two sensors is significant, only targets with relatively smooth spectra profiles will be selected as PIPs. Similarly, when one sensor contains an atmospheric absorption feature within the SRF and the other does not, only targets that are not susceptible to atmospheric influence are selected as PIPs.

Consider two sensors with $N$ matching bands for intercalibration. An image pair of two observations of the common targets from the two sensors can be represented by a random vector $\mathbf{F} = (F_1, \ldots, F_N)^{\mathrm{T}}$ and $\mathbf{G} = (G_1, \ldots, G_N)^{\mathrm{T}}$, respectively. Nielsen et al. [32] proposed that the MAD variates can be determined by a linear transformation of $\mathbf{F}$ and $\mathbf{G}$ with coefficients vector $\mathbf{a}$ and $\mathbf{b}$, and the maximum variance of the MAD variates is achieved

$$U = \mathbf{a}^{\mathrm{T}}\mathbf{F} = a_1 F_1 + a_2 F_2 + \ldots + a_N F_N \quad (11)$$

$$V = \mathbf{b}^{\mathrm{T}}\mathbf{G} = b_1 G_1 + b_2 G_2 + \ldots + b_N G_N \quad (12)$$

$$\mathrm{MAD}_i = U_i - V_i = \mathbf{a}_i^{\mathrm{T}}\mathbf{F} - \mathbf{b}_i^{\mathrm{T}}\mathbf{G}, \quad i = 1, \ldots, N \quad (13)$$

where the coefficients vector $\mathbf{a}$ and $\mathbf{b}$ can be resolved by applying standard canonical correlation analysis (CCA) [38]. There are some underlying properties for MAD variates: 1) from the central limit theorem, the MAD variates, determined by several additions and subtractions, would ideally fit a normal distribution; and 2) since MAD variates are orthogonal (uncorrelated), all the MAD variates should follow

a multivariate normal distribution with diagonal covariance matrix [36].

Let the random variable $Z$ represent the sum of squares of standardized MAD variates

$$Z = \sum_{i=1}^{N} \left(\frac{\mathrm{MAD}_i}{\sigma_i}\right)^2 \quad (14)$$

where $\sigma_i$ is the variance of $\mathrm{MAD}_i$. Then, $Z$ should follow a chi-square distribution with $N$ degrees of freedom ($\chi_N^2(z)$). An iteration scheme is adopted by setting the probability of no change of observations as the weight for the next MAD transformation. The probability of no change of observations $z$ can be determined by the chi-square distribution as follows:

$$P_{\mathrm{no\_change}}(z) = 1 - \chi_N^2(z). \quad (15)$$

The general idea behind this formulation is that a small $z$ implies a high probability of no change, resulting in a large weight in the next iteration. This can be considered as more emphasis placed on establishing a better background for detecting change against a background of no change, therefore resulting in improved sensitivity of the MAD transformation [36].

The iteration of MAD transformation will continue until one of the following conditions is met: 1) maximum number of iterations reached, usually set to 30; and 2) the largest absolute change in the canonical correlations, i.e., correlations of $U$ and $V$, becomes smaller than some preset small value (e.g., $10^{-6}$). Once the iteration ceases, a decision threshold $k$ can be made to choose the final PIPs for intercalibration. Typically, the $k$ is set to be the value of $z$ when $P_{\mathrm{no\_change}}(z) = 0.9$, that is, pixels which satisfy $P_{\mathrm{no\_change}}(z) > 90\%$ are designated as PIPs.

The PIPs are selected statistically from the image pair without a priori knowledge of the target pixel. They should correspond to truly invariant targets for which the overall differences between the image pair can be attributed to linear effects as expressed in (9). The location of the PIPs is likely to change with each image pair, which is reasonable because whether a target is designated as PIP is affected by the atmospheric condition as well as the BRDF effect besides its own spectral signature.

With the selected PIPs, an orthogonal, as opposed to ordinary, linear regression can be performed on the PIPs as demonstrated by [33]. The regression slope $m_i(t)$ provides a measurement of $(f_0 \cdot f_{\mathrm{SBAF}}/S_{Vi}(t))$ as shown in (9). By performing the IR-MAD procedure on image pairs from different acquisition times, a large database of $m_i(t)$ can be created. Analysis of these data can provide long-term intercalibration results of the two sensors, which can be seen in Section V.

In summary, the steps involved in IR-MAD for intercalibration are as follows.

1) Reproject the near-simultaneous overpass at the ROI from the two sensors onto a common geographic grid to get the image pair.
2) Start with the original MAD transformation for the image pair, i.e., set weights = 1 for all pixels.
3) Iterate the MAD procedure until termination conditions are met as follows.
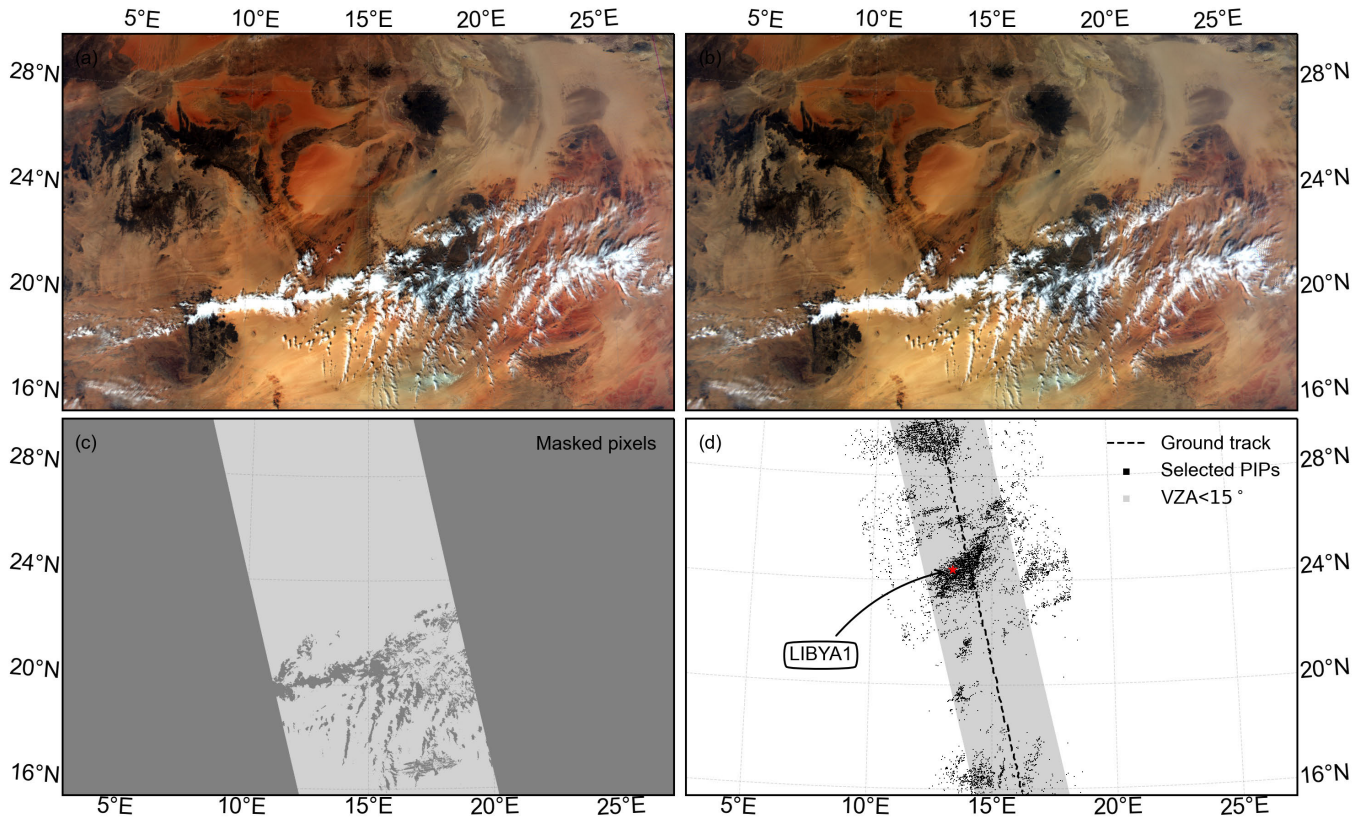
Fig. 3. True color images at the ROI from (a) FY-3B/MERSI and (b) FY-3B/VIRR on 20110123. (c) Mask used for statistical analysis of MAD method. (d) Spatial distribution of selected PIPs from IR-MAD method, only the pixels with VZA < 15° are used for regression. PIPs: pseudo-invariant pixels; VZA: view zenith angle.

   a) Set the probability of no change from the last MAD procedure as the weight for all pixels.

   b) Perform the MAD procedure on the reweighted image pair.

   c) Calculate weights for the next iteration.

4) Select PIPs from the last MAD procedure by the preset decision threshold $k$.

5) Perform an orthogonal regression on PIPs to get regression slope $m_i$, which is a measurement of the intercalibration result.

## IV. IMPLEMENTATION AND ANALYSIS

### A. Examples Applied on FY-3 VIRR

The long-term time series datasets of MERSI and VIRR onboard FY-3A and FY-3B satellites are created by reprojecting the L1B data onto a common geographic grid in 1km spatial resolution via the nearest neighbor method. This is a prerequisite for making pair-wise comparisons for the IR-MAD procedure. A rough threshold-based cloud detection algorithm is applied to remove cloud pixels. Nevertheless, it must be acknowledged that the reduction of variations in the scene can improve the sensitivity of the MAD procedure, the IR-MAD method statistically and iteratively selects the true PIPs hence delicate cloud detection is not necessary.

Our method assumes that the radiometric difference between the PIPs from an image pair is solely due to the linear effects

as shown in (9), thus other possible causes of change, such effects as BRDF and misregistration, need to be eliminated or at least minimized. Since the two sensors are onboard the same platform, the difference due to the BRDF effect is negligible. In order to reduce the uncertainty introduced by misregistration error, only pixels with view zenith angle (VZA) < 30° are used for statistical analysis of IR-MAD and pixels with VZA < 15° are selected as PIPs for orthogonal regression. This is mainly because a large geolocation error exists and the spatial size of pixels increases at the edge of the swath. The impact of different VZAs and scattering regimes was examined in [34].

Once the image pair data are masked as described above, the IR-MAD procedure is applied subsequently to determine the set of PIPs, of which the number can be up to several thousand. The number of PIPs of each image pair varies with the present atmospheric and surface conditions. In order to exclude image pairs strongly affected by the atmosphere, image pairs with PIPs number less than 1000 or a regression correlation less than 0.95 will be removed. This means that the differences between these image pairs no longer conform to the linear effects due to atmospheric or surface influences and therefore are not suitable for intercalibration analysis.

Fig. 3 shows an implementation of the IR-MAD method applied to FY-3B for intercalibration on January 23, 2011. Fig. 3(a) and (b) shows the true color images of MERSI and VIRR, respectively. The image of MERSI looks a little redder
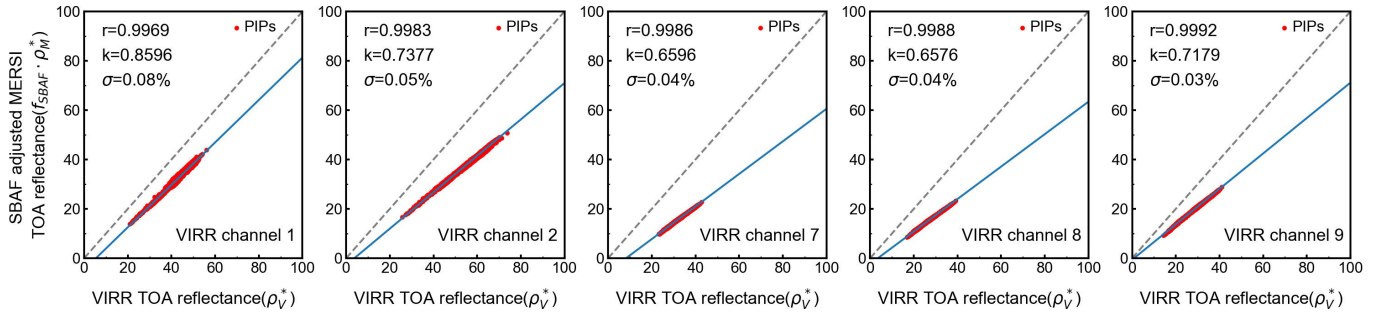
Fig. 4. Regression results of the PIPs selected by IR-MAD on 20110123. The number of PIPs is 7387. PIPs: pseudo-invariant pixels; $r$: correlation coefficient; $k$: regression slope; and $\sigma$: uncertainty (one-sigma error) of $k$.

than that of VIRR, which is mainly caused by the difference in SRFs. Fig. 3(c) presents the mask used before the IR-MAD procedure, and the spatial distribution of selected PIPs is shown in Fig. 3(d). Interestingly, it can be seen that the CEOS-defined PICS, LIBYA1, is automatically selected as PIPs. This suggests that LIBYA1 is indeed a very suitable PICS for intercalibration, and also proves the efficacy of our method to accurately select PIPs. A potential advantage of using IR-MAD to select targets is that besides the traditional sites used for calibration, which generally have few surface types and limited reflectance dynamic range, the IR-MAD can automatically select thousands of PIPs with various spectral signatures over a wider radiance dynamic range including the lower reflectance targets (see the spatial distribution of PIPs and their corresponding surface types in Fig. 3).

PIPs selected by the IR-MAD method can then be used in linear regression to obtain the slope $m_i$ for all bands, which is a measurement of the calibration difference between MERSI and VIRR. Fig. 4 shows the regression result of the PIPs in Fig. 3. Note that the MERSI nominal TOA reflectance ($\rho_M^*$) has been compensated by $f_{SBAF}$ for comparison. The regression intercept is due to the unaccounted for change in the zero-radiance response of VIRR after launch, which makes the prelaunch coefficients unable to accurately measure its zero-radiance response on orbit. Though the PIPs are spatially dispersed and consist of a variety of surface targets, the correlation coefficient ($r$) values and the dynamic range covered in the plot clearly indicate the benefit of using PIPs for radiometric intercalibration. The $r$ values for all bands are in excess of 0.99, and the uncertainties (one-sigma error) of regression slopes are all less than 1%. The regression results demonstrate that PIPs can be well used for intercalibration and can accurately measure the calibration difference between the two sensors.

The ROI in this study has a large spatial range, about 2600 km horizontally and 1600 km vertically. Due to the constraint of VZA in the IR-MAD procedure, the spatial distribution of PIPs in a single day is limited and cannot be spread over the entire ROI. Given the nominal revisit cycle of FY-3A/B is 5.5 days, assuming that the sensor radiometric calibration is stable during the period, it is reasonable to aggregate PIPs from five consecutive days to further enhance the abundance of targets and dynamic range. Fig. 5 presents two examples of the spatial distribution of aggregated PIPs at the

early and later stages of FY-3B's lifecycle. Although the orbit of the satellite has drifted during this period and the sensor has also experienced relatively large degradation, the spatial distribution of PIPs is consistent except in some cloud areas. This means that whether a target is selected as PIPs depends on the intrinsic properties of the target, which has nothing to do with the radiometric performance of the sensors.

Fig. 6 shows the regression results of the aggregated PIPs from five consecutive days. In contrast to single-day PIPs for regression in Fig. 4, the five-day aggregated PIPs do not deviate from each other and still converge to the same linear relationship. What is more, the regression results of aggregated PIPs have a wider reflectance dynamic range for all bands, and the uncertainty of the regression slope is no more than 0.4%. These superiorities indicate that it is reasonable and necessary to aggregate multiday PIPs for regression analysis, especially for long-term intercalibration with a time span of several years.

### B. IR-MAD Versus SNO-x

The most related work to our study is the SNO-$x$ method, which extends the SNO analysis to the low latitude desert and ocean sites, and sets a number of criteria to choose spatially uniform ROIs to evaluate the bias between two sensors [8]. In this study, based on the potential linear relationship between two sensors, the IR-MAD technique was used to statistically select PIPs to intercalibrate the sensor. Here, we compare the performance of the IR-MAD-based method and the SNO-$x$-based method for intercalibration. There are multiple criteria established to select the ROIs for SNO-$x$ analysis as outlined in the original paper [8], including: 1) scan angle difference, time difference, and closest-matching distance limit for geospatial matching. These are inherently satisfied as the two sensors used for intercomparison are onboard the same satellite; 2) the size of the ROI is 9 × 9 km, the solar zenith is less than 80° and the spatial uniformity should be less than 2%. These criteria align with those in the original paper; and 3) the VZA is restricted to within 15° to ensure a fair comparison with the IR-MAD method. We set the moving stride to 5 (which means there is overlap) to increase the number of regression samples. The mean reflectance for each ROI is calculated for regression.

Fig. 7 shows a comparison of the spatial distribution of matched pixels selected by two methods on January 21, 2011.
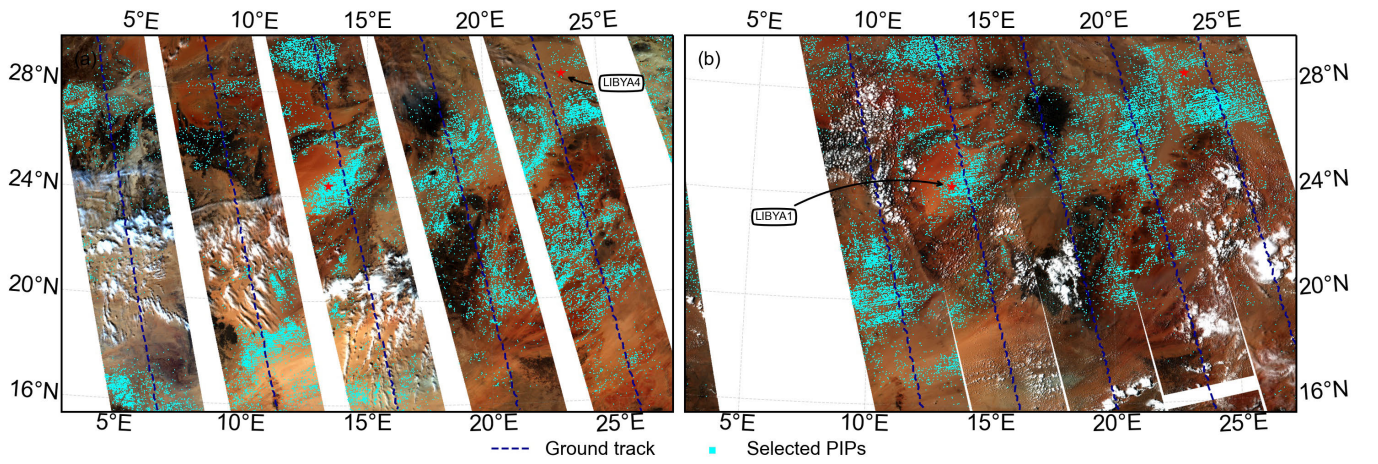
Fig. 5. Aggregated PIPs selected by IR-MAD overlay the concurrent true color images (VZA < 15°) of FY-3B/MERSI from five consecutive days: (a) 20110121–20110125 at early stage of FY-3B's lifecycle and (b) 20180728–20180801 in the later of FY-3B's lifecycle.
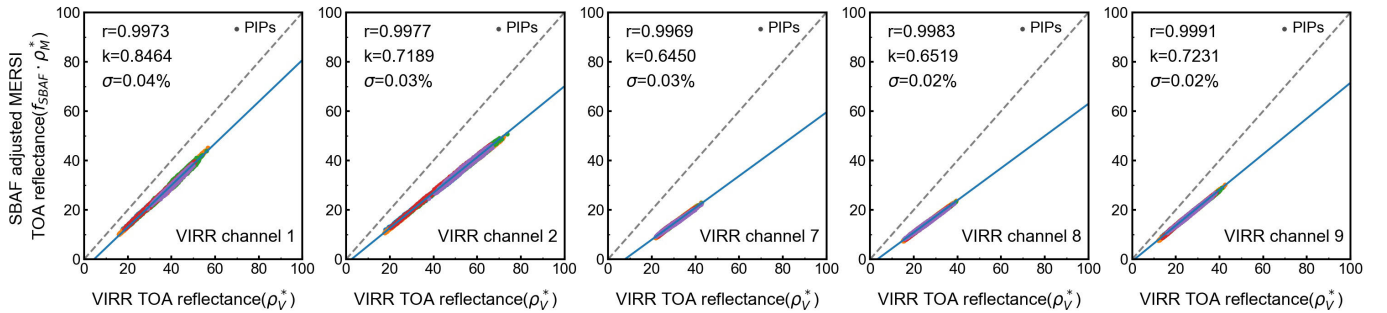


Fig. 6. Regression results of the aggregated PIPs selected by IR-MAD from five days (20110121, 20110122, 20110123, 20110124, and 20110125). Different colored dots represent PIPs from different days. The total number of PIPs is 29171.
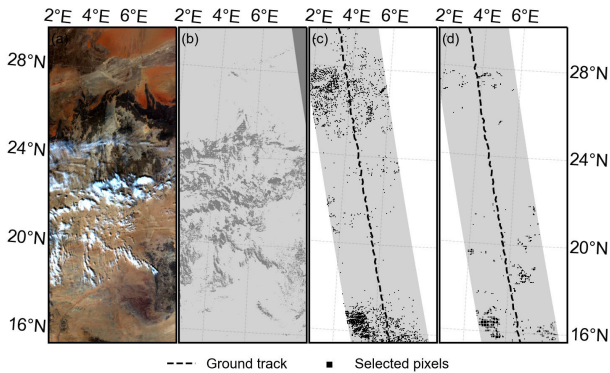


Fig. 7. Comparison of the spatial distribution of pixels selected by the SNO-$x$ and IR-MAD methods on 20110121. (a) True color image from FY-3B/MERSI. (b) Mask used before selection. (c) Pixels selected by IR-MAD method. (d) Pixels selected by SNO-$x$ method. The gray area in (c) and (d) represents the area where the VZA < 15°.

The main reason for choosing this case is that it covers diverse land cover types, rather than a homogeneous desert area, which better reflects the superiority of our method. Fig. 7 illustrates that in scenes containing complex samples, the SNO-$x$ method selects fewer spatially uniform ROIs and the sample type is relatively small, mainly comprising desert targets. In contrast, the IR-MAD method can automatically select appropriate PIP-level samples

for regression without requiring spatial uniformity, resulting in a greater number of samples with a wider range of types.

Fig. 8 presents the regression results of the selected samples from one day by the two methods. It can be seen intuitively that the TOA reflectance of the regression samples selected by the IR-MAD method has a wider dynamic range, indicating a greater diversity in the selected samples. Furthermore, while the SNO-$x$ method selects samples with overlapping, the number of samples is fewer than with IR-MAD, particularly in more complex scenes, e.g., those with higher cloud coverage where it is challenging to obtain large spatially uniform regions. With regards to regression results, the IR-MAD method has a very consistent regression slope with the SNO-$x$ method, and the uncertainty of the regression slope is smaller, which also confirms the correctness of the samples selected by the IR-MAD method.

Table III presents the comparison of regression results obtained by applying the SNO-$x$ method and the IR-MAD method from five consecutive days. It is evident that the IR-MAD method has significant advantages over the SNO-$x$ method in terms of the number of regression samples, the dynamic range of TOA reflectance for each channel, and the uncertainty of the regression slope. Moreover, this method requires no prior knowledge of the surface and is globally applicable.
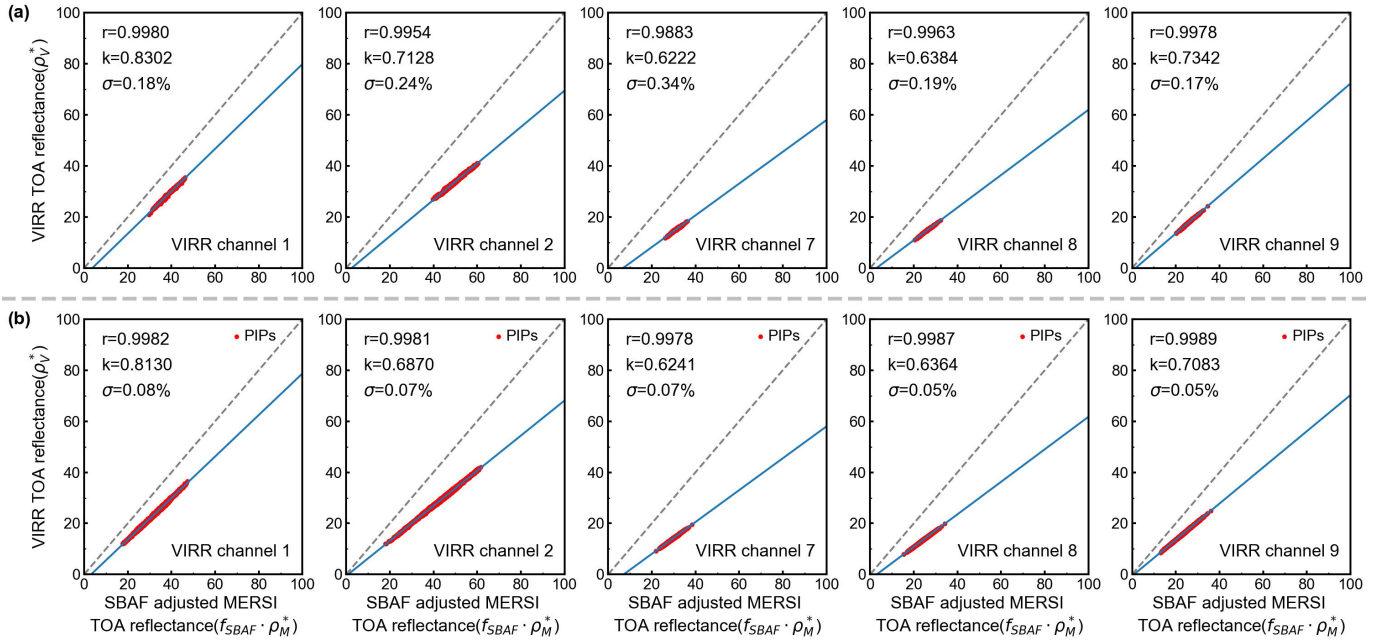
Fig. 8. Comparison of the regression results for FY-3B on 20110121, where the samples are selected by the two different methods: (a) SNO-$x$, with 812 samples; and (b) IR-MAD method, with 3175 samples.

TABLE III
COMPARISON OF REGRESSION RESULTS OBTAINED BY APPLYING THE SNO-$x$ METHOD AND THE IR-MAD METHOD FOR FY-3B OVER FIVE CONSECUTIVE DAYS

| date | method | number of samples | channel 1 | | channel 2 | | channel 7 | | channel 8 | | channel 9 | |
|---|---|---|---|---|---|---|---|---|---|---|---|---|
| | | | $\sigma(\%)$ | range [min, max] | $\sigma(\%)$ | range [min, max] | $\sigma(\%)$ | range [min, max] | $\sigma(\%)$ | range [min, max] | $\sigma(\%)$ | range [min, max] |
| 20110121 | SNOX-$x$ | 812 | 0.18 | [29.6, 46.2] | 0.24 | [39.6, 60.5] | 0.34 | [26.1, 36.3] | 0.19 | [20.4, 32.2] | 0.17 | [20.1, 34.6] |
| | IR-MAD | 3875 | 0.08 | [17.6, 47.3] | 0.07 | [17.9, 61.7] | 0.07 | [21.9, 38.5] | 0.05 | [15.5, 34.3] | 0.05 | [13.1, 36.0] |
| 20110122 | SNOX-$x$ | 3007 | 0.1 | [32.9, 56.9] | 0.05 | [41.8, 72.6] | 0.06 | [26.7, 42.5] | 0.03 | [21.1, 39.5] | 0.04 | [20.9, 42.8] |
| | IR-MAD | 4307 | 0.05 | [15.9, 56.6] | 0.02 | [17.6, 72.1] | 0.04 | [21.7, 42.6] | 0.03 | [15.1, 39.5] | 0.04 | [12.0, 42.6] |
| 20110123 | SNOX-$x$ | 3436 | 0.21 | [30.4, 57.9] | 0.12 | [42.7, 75.7] | 0.06 | [25.2, 41.5] | 0.05 | [19.9, 37.9] | 0.05 | [19.4, 40.7] |
| | IR-MAD | 7387 | 0.08 | [20.8, 56.1] | 0.05 | [25.7, 73.7] | 0.04 | [23.2, 42.8] | 0.04 | [16.8, 39.2] | 0.03 | [14.3, 41.1] |
| 20110124 | SNOX-$x$ | 2822 | 0.12 | [31.2, 50.6] | 0.11 | [40.7, 66.1] | 0.08 | [25.9, 42.4] | 0.07 | [20.6, 36.7] | 0.08 | [21.4, 37.8] |
| | IR-MAD | 5203 | 0.08 | [18.3, 50.6] | 0.05 | [20.3, 66.4] | 0.07 | [22.3, 40.9] | 0.05 | [16.0, 36.7] | 0.05 | [13.6, 38.5] |
| 20110125 | SNOX-$x$ | 5991 | 0.13 | [32.4, 50.1] | 0.2 | [42.1, 66.8] | 0.06 | [24.8, 42.2] | 0.06 | [19.5, 37.9] | 0.05 | [20.3, 37.6] |
| | IR-MAD | 8399 | 0.1 | [29.0, 49.9] | 0.09 | [37.7, 66.9] | 0.04 | [21.9, 42.7] | 0.04 | [15.9, 38.3] | 0.04 | [15.9, 37.9] |

$\sigma$: uncertainty (one-sigma error) of regression slope.
range: TOA reflectance range of regression samples.

## V. RESULTS

### A. Long-Term Time Series Results of FY-3A&3B VIRR

By performing the IR-MAD procedure on all image pairs and subsequently aggregating five-day PIPs for regression, a large database of $m_i(t)$ can be created. Note that the MERSI nominal TOA reflectance ($\rho_M^*$) has been compensated by $f_{SBAF}$ before, thus the $m_i(t)$ here represents the measurement of $(f_0/S_{Vi}(t))$. For FY-3A data with a time span of six years, there are 439 five-day comparisons, and for FY-3B data with a time span of eight years, there are a total of 564 five-day comparisons. Analysis of these data can provide long-term intercalibration results for the two sensors.

The long-term time series of $m_i(t)$ for FY-3A and FY-3B are shown in Fig. 9. The gaps in the curves are due to missing data. It can be seen that there is a decreasing trend in all bands for both sensors. This is because all bands of VIRR have different degrees of degradation. In addition to long-term trends, periodic seasonal oscillations exist in some bands, especially for channels 1 and 2. Examination of the fitting error and potential overfitting problem shows that a polynomial of order 4 can best capture the trending pattern. For the regression intercepts in each comparison, they are attributed to the unaccounted for change in the zero-radiance response of VIRR after launch, which should generally remain stable over time in orbit. However, due to the degradation of VIRR itself, there would be a trend in the regression intercepts iover time (not shown). In this study, we employed a second-order polynomial fitting to capture the trend of the regression intercept for correction. The coefficients of the fit polynomials and bias statistics can be seen in Table IV.

As mentioned above, the $m_i(t)$ is a measurement of the relative calibration factor ($f_0$) and the sensor degradation ($1/S_{Vi0}$). The VIRR degradation can be obtained independently by the approach of [28] and [34]. Therefore, we can obtain the relative calibration factor ($f_0$) by dividing $m_i(t)$ by sensor
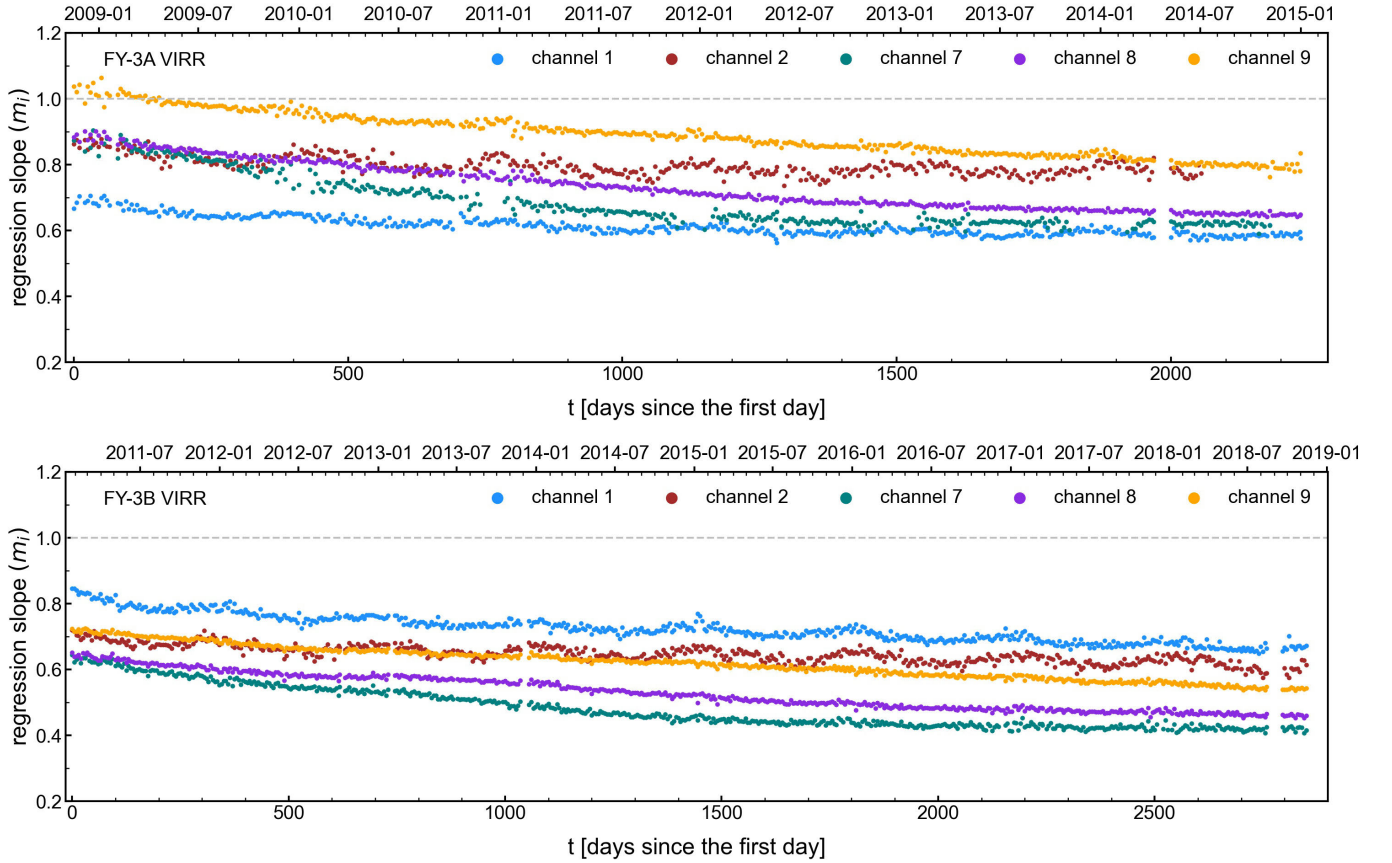
Fig. 9. Long-term time series of regression slope [$m_i(t)$] for FY-3A and FY-3B, which is a measurement of the relative calibration factor between MERSI and VIRR and the sensor degradation of VIRR itself.

TABLE IV
COEFFICIENTS OF THE FIT POLYNOMIALS FOR LONG-TERM TIME SERIES OF $m_i(t)$ AND REGRESSION OFFSET, ALONG WITH THE FITTING BIAS STATISTICS FOR $m_i(t)$

| VIRR band | $m(t) = a_0 + a_1 t + a_2 t^2 + a_3 t^3 + a_4 t^4$ | | | | | $offset(t) = b_0 + b_1 t + b_2 t^2$ | | | bias mean (%) | bias std (%) |
|---|---|---|---|---|---|---|---|---|---|---|
| | $a_0$ | $a_1(\times 10^{-4})$ | $a_2(\times 10^{-7})$ | $a_3(\times 10^{-11})$ | $a_4(\times 10^{-14})$ | $b_0$ | $b_1(\times 10^{-4})$ | $b_2(\times 10^{-7})$ | | |
| fy3a/ch1 | 0.6858 | -1.5767 | 1.1953 | -4.7703 | 0.7568 | -2.2214 | 8.1813 | -3.6872 | 0.0001 | 1.6394 |
| fy3a/ch2 | 0.8554 | -1.4257 | 1.1732 | -5.2327 | 1.0301 | -2.4014 | 16.315 | -8.1611 | 0.0000 | 2.3243 |
| fy3a/ch7 | 0.8856 | -3.2868 | 0.5078 | 6.8015 | -2.2115 | -5.0486 | 28.606 | -14.152 | 0.0001 | 1.8337 |
| fy3a/ch8 | 0.8848 | -1.8592 | 0.2292 | 0.9403 | -0.1600 | -7.9868 | 4.1352 | -2.0237 | 0.0000 | 0.8153 |
| fy3a/ch9 | 1.0283 | -2.2065 | 1.4163 | -6.5519 | 1.1270 | -5.6542 | 21.537 | -7.2687 | 0.0000 | 1.0514 |
| fy3b/ch1 | 0.8261 | -1.9008 | 1.5373 | -6.3876 | 0.9259 | -2.6697 | -2.6514 | -0.1468 | 0.0000 | 1.5873 |
| fy3b/ch2 | 0.6977 | -0.8124 | 5.0772 | -1.6215 | 0.1562 | -1.2840 | 3.5416 | 0.6355 | 0.0000 | 2.3130 |
| fy3b/ch7 | 0.6264 | -1.5049 | -0.0252 | 2.3268 | -0.4491 | -4.4480 | 9.0079 | -2.7429 | -0.0005 | 1.5665 |
| fy3b/ch8 | 0.6376 | -1.0266 | 0.3000 | -1.5524 | 0.3598 | -2.0573 | 1.8634 | -0.5125 | 0.0002 | 1.2841 |
| fy3b/ch9 | 0.7232 | -1.4534 | 0.9793 | -4.2652 | 0.6441 | -1.0563 | -0.9416 | -0.3341 | 0.0000 | 0.7523 |

degradation ($1/S_{Vi0}$). Fig. 10 shows the long-term time series of $f_0$. Since we used fixed calibration coefficients at the early operational stage to calculate the nominal TOA reflectance, $f_0$ represents the relative calibration factor of the two sensors at that time, which is expected to be a constant. Due to the limitations of the polynomial functions used to fit the $m_i(t)$ and sensor degradation ($1/S_{Vi0}$) trending, they cannot fully capture the seasonal variation. Consequently, periodic seasonal oscillations may manifest in the time series of the $f_0$. We tried to fit the trending of $f_0$ with polynomials of different orders, all tend to be a constant (as expected), which demonstrates the validity of the time series of $m_i(t)$ we derived.

Furthermore, we can utilize the estimated $f_0$ value to calculate the VIRR degradation and compare it with our previous

work [28]. Unlike the IR-MAD technique applied in this study for intercalibration, the IR-MAD technique is proposed to select temporally invariant pixels from the bitemporal satellite images by the same sensor to assess the sensor response degradation during the acquisition time interval [28]. By dividing the polynomials of $m_i(t)$ by the estimated $f_0$, we can obtain the sensor degradation as a function of time. The outcomes are depicted in Fig. 11, where the solid lines correspond to the degradation calculated in this study, and the dashed lines represent the outcomes obtained using the method of [28]. The highly consistent VIRR degradation curves obtained from the two methods further confirm the effectiveness of this approach.

Table V presents a quantitative comparison of the degradation results of VIRR obtained in this study with those
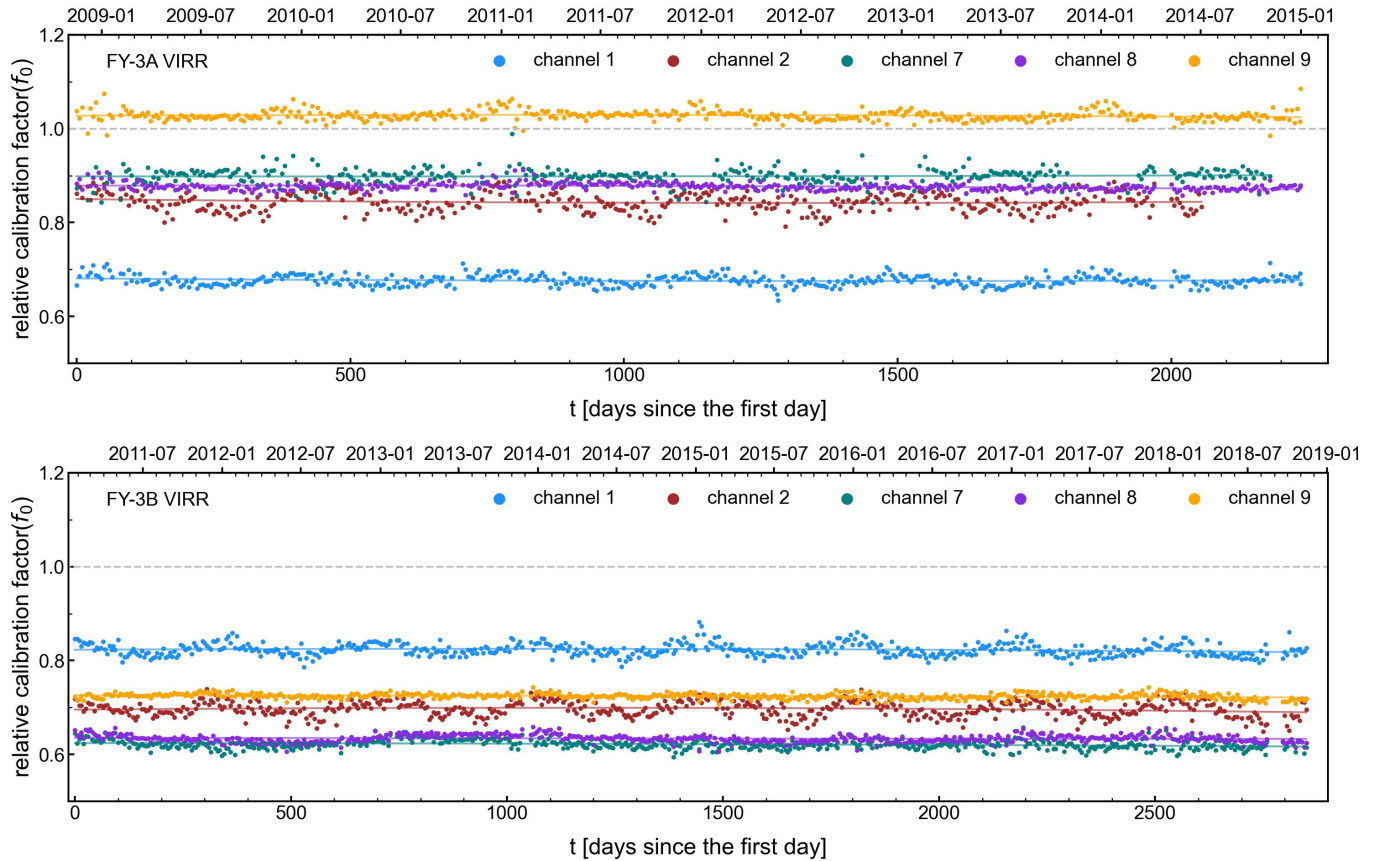
Fig. 10. Long-term time series of relative calibration factor ($f_0$) for FY-3A and FY-3B, which expects to be a constant. See main text for more explanation about $f_0$.

from the other two different methods, including a multisite calibration method [39], [40] and an IR-MAD based method for sensor degradation tracking [28], and their results have been unified to the same time range. It can be seen that the degradation results of VIRR obtained in this study are very consistent with the other methods. Compared to the results of the other two methods, the annual degradation for most channels differs by less than 0.1%. For channels with significant seasonal fluctuations (such as channel 2), the difference can reach around 0.3%. As for channel 7, which is a short-wave channel, it is strongly affected by atmospheric absorption and scattering, resulting in a difference of around 0.5%. This verifies the consistency of the VIRR degradation results obtained by this method with other methods.

### B. TOA Reflectance Trending Validation Over PICS

As an independent calibration method of on-orbit calibration, ground sites with suitable characteristics on Earth are often used to evaluate and validate the postlaunch radiometric performance of satellite sensors. Monitoring the long-term time series of TOA reflectance at PICS is an effective approach to verifying the radiometric calibration consistency between different sensors. In the ROI of this study, there are two PICS identified by the CEOS, namely, LIBYA1 and LIBYA4. They are desert sites consisting of sand dunes and devoid of

vegetation. These sites have been extensively studied and used as postlaunch calibration sites for satellite optical sensors to evaluate the long-term stability and intercomparisons. Due to space limitations, the long-term time series of TOA reflectance over Libya 4 for FY-3B are presented here. FY-3B was selected due to its longer time span, and LIBYA4 has been the most commonly used calibration site in recent years. Similar results can also be obtained for FY-3A and LIBYA1, which will be presented in the table.

By selecting clear-sky samples with a sensor zenith angle less than 20° during satellite overpasses, Fig. 12 shows the long-term time series of the TOA reflectance of FY-3B/VIRR over LIBAYA4 before and after intercalibration, with the MERSI used as a reference. To mitigate seasonal oscillations arising from the BRDF effect or orbital drift, the TOA reflectance has been characterized by the solar zenith angle and normalized to the TOA reflectance at a solar zenith angle of 30°. From the figure, it can be observed that before intercalibration, due to the degradation of the VIRR itself, there is a significant downward trend in each channel, while MERSI as the reference sensor has a very stable and flat long-term response. After intercalibration, the trend of VIRR has been eliminated and it has a consistent radiometric response with MERSI, indicating that our intercalibration method is effective. The second column of Fig. 12 shows the relative deviation of TOA reflectance between MERSI and intercalibrated VIRR, which exhibits a seasonal oscillations
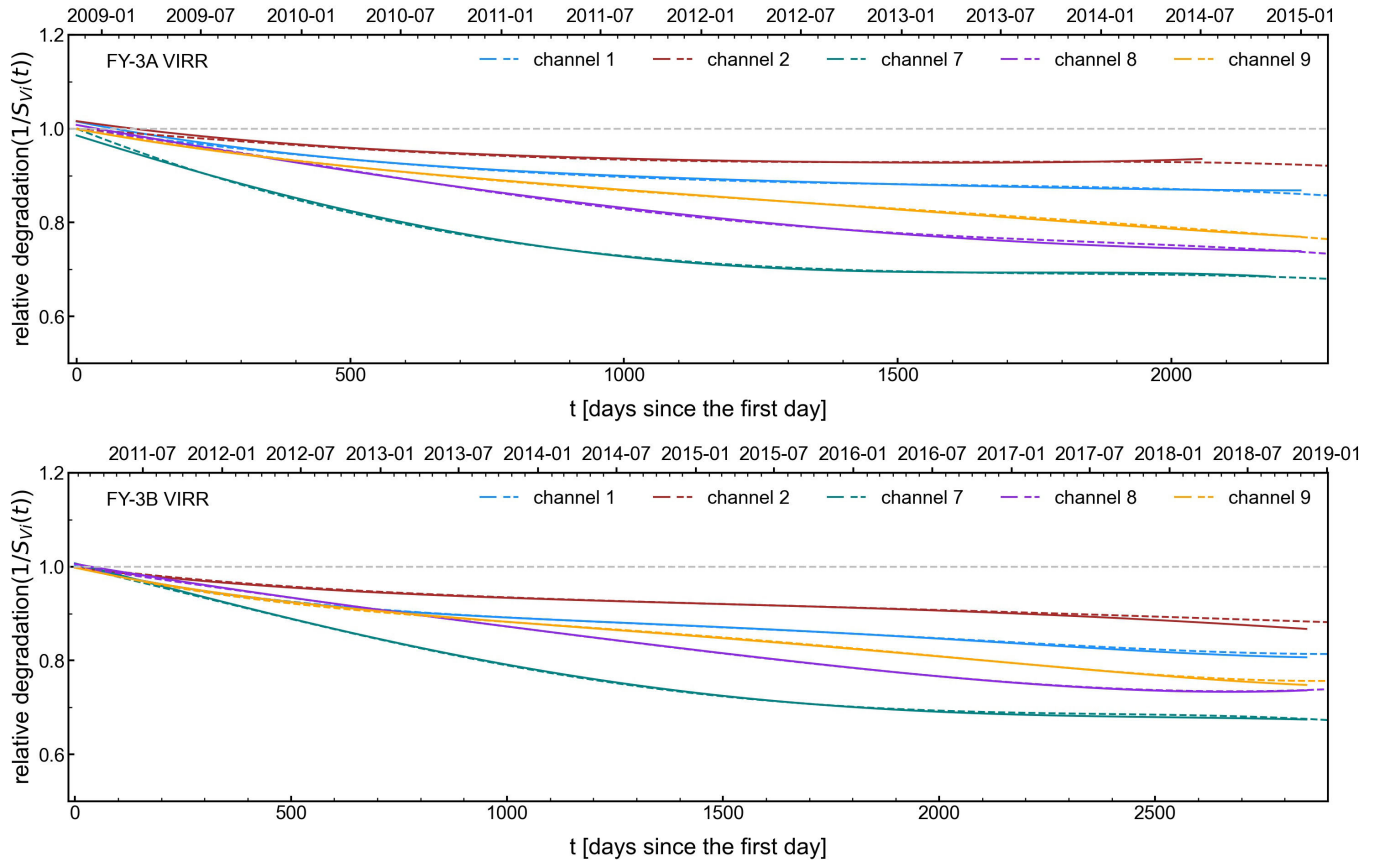
Fig. 11. Degradation curves over time of the VIRR on FY3A and FY3B. The solid lines correspond to the degradation obtained in this study and the dashed lines represent the results using the method of [28].

TABLE V

COMPARISON OF THE TOTAL AND ANNUAL DEGRADATION OF VIRR OBTAINED USING THREE DIFFERENT METHODS. FY3A: FROM NOVEMBER 16, 2008, TO DECEMBER 1, 2014. FY3B: FROM JANUARY 25, 2011, TO DECEMBER 1, 2017

| VIRR band | total degradation | | | annual degradation | | |
|---|---|---|---|---|---|---|
| | method 1 ( [39]) | method 2 ( [28]) | this study | method 1 ( [39]) | method 2 ( [28]) | this study |
| fy3a/ch1 | 14.06% | 13.74% | 14.44% | 2.33% | 2.27% | 2.39% |
| fy3a/ch2 | 9.48% | 7.58% | 7.17% | 1.57% | 1.25% | 1.19% |
| fy3a/ch7 | 30.26% | 31.66% | 30.66% | 5.01% | 5.24% | 5.07% |
| fy3a/ch8 | 27.11% | 26.02% | 26.62% | 4.49% | 4.31% | 4.40% |
| fy3a/ch9 | 22.18% | 22.81% | 22.76% | 3.67% | 3.77% | 3.77% |
| fy3b/ch1 | 18.08% | 17.65% | 18.26% | 2.64% | 2.57% | 2.66% |
| fy3b/ch2 | 13.54% | 10.64% | 11.20% | 1.98% | 1.55% | 1.63% |
| fy3b/ch7 | 35.67% | 31.54% | 32.54% | 5.20% | 4.60% | 4.75% |
| fy3b/ch8 | 28.34% | 26.30% | 26.85% | 4.13% | 3.84% | 3.92% |
| fy3b/ch9 | 23.07% | 23.03% | 22.99% | 3.37% | 3.36% | 3.35% |

pattern. The pattern becomes more pronounced in the later stage of the satellite's life cycle, which may be related to the orbital drift of FY-3B in its later phase. Table VI presents the quantitative results of the relative deviation between MERSI and intercalibrated VIRR on FY-3A and FY-3B over LIBIYA1 and LIBAYA4. It can be seen that for most channels, the mean deviation is less than 1%, with a standard deviation of less than 2%. For some channels with significant seasonal fluctuations, the deviation may be slightly larger, but the mean deviation is also less than 2%, with a standard deviation of less than 2.5%. The mechanism behind the significant seasonal fluctuations and amplitude of TOA reflectance bias

will be further investigated. The quantitative results of the two satellites over the two PICS have also verified the accuracy and effectiveness of our method.

### C. Uncertainty Analysis

In this intercalibration, the uncertainty primarily originates from the radiometric calibration uncertainty of the reference sensor and the processing procedure of the intercalibration. Here, we mainly analyze the uncertainty introduced by several factors in our processing method, including: geometric mis-registration, spectral band differences, atmospheric conditions,
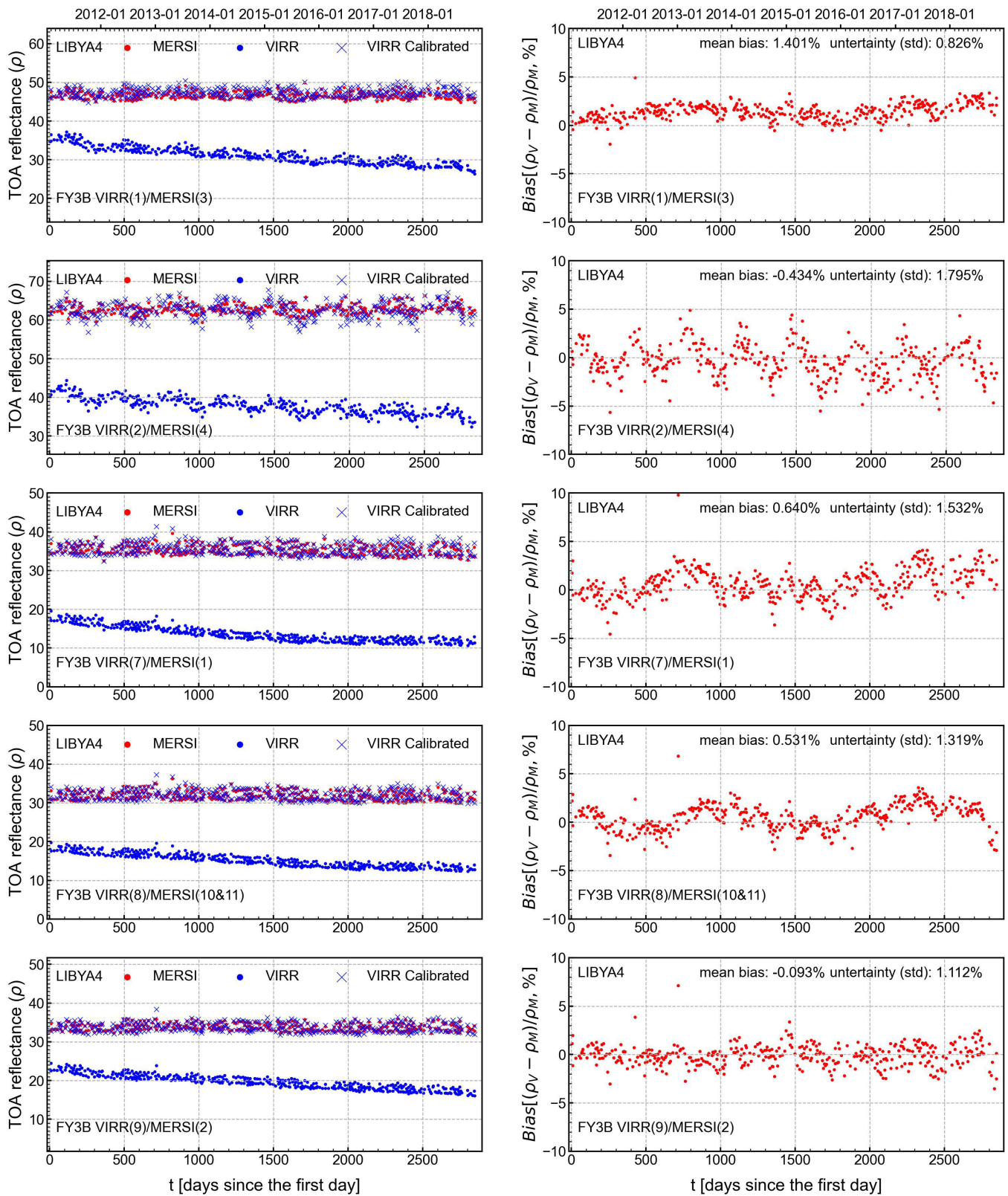
Fig. 12. Long-term time series of the TOA reflectance of FY-3B/VIRR over LIBAYA4 before and after intercalibration, with the MERSI used as a reference. The second column shows the relative deviation of TOA reflectance between MERSI and intercalibrated VIRR.

and viewing geometry (or BRDF) effects during overpass. In this study, since the two sensors are onboard the same platform, the differences caused by atmospheric conditions and BRDF effects are negligible.

TABLE VI

QUANTITATIVE RESULTS OF THE RELATIVE DEVIATION BETWEEN MERSI AND INTERCALIBRATED VIRR ON FY-3A AND FY-3B OVER LIBYA1 AND LIBYA4

| VIRR band | LIBYA1 | | LIBYA4 | |
|---|---|---|---|---|
| | bias mean | bias std | bias mean | bias std |
| fy3a/ch1 | -0.578% | 0.866% | 0.845% | 0.888% |
| fy3a/ch2 | 0.725% | 1.623% | -1.200% | 1.626% |
| fy3a/ch7 | 0.667% | 1.550% | -0.790% | 1.297% |
| fy3a/ch8 | 1.009% | 1.096% | -0.371% | 0.915% |
| fy3a/ch9 | 0.767% | 1.034% | -0.654% | 0.872% |
| fy3b/ch1 | -1.399% | 0.855% | 1.401% | 0.826% |
| fy3b/ch2 | 0.479% | 1.787% | -0.434% | 1.795% |
| fy3b/ch7 | 1.480% | 1.750% | 0.640% | 1.532% |
| fy3b/ch8 | 1.341% | 1.360% | 0.531% | 1.319% |
| fy3b/ch9 | 0.557% | 1.213% | -0.093% | 1.112% |



Fig. 13. Density map of the spatial frequency distribution of PIPs for all image pairs of FY-3B.

MERSI and VIRR have little difference in spatial resolution, making it challenging to achieve perfect pixel matching between the two sensors, especially in off-nadir areas. To minimize the effects of different spatial resolutions, our method limits the near-nadir (VZA≤15) pixels for analysis and regression. Furthermore, the IR-MAD technique statistically selects PIPs that satisfy the underlying linear relationship [see (9)] in each channel, hence pixels with larger differences due to misregistration will not be selected as PIPs. As a result, in the presence of a misregistration effect, IR-MAD tends to select PIPs from spatially uniform areas. Similarly, when atmospheric disturbances and BRDF effects are present, IR-MAD also tends to select pixels with the smallest possible impact of these effects. Thus, the uncertainty introduced by these effects is implicitly reduced during the PIPs selection of IR-MAD.

One of the primary sources of uncertainty in our method is the differences in RSRs. Despite compensating with SBAF, the SBAFs for different land cover types are not the same. Hence, when the study area is vast and encompasses diverse land cover types, IR-MAD favors selecting pixels with flat spectral signatures to minimize such effects.

The uncertainty arising from the above effects is reflected in the residual standard deviation of the regression results. For the 439 five-day comparisons of FY-3A and the 565 five-day comparisons of FY-3B, the mean uncertainty for the matching bands are listed on the first row of Table VII. For long-term intercalibration results, additional uncertainties are introduced by polynomial fitting, mainly due to seasonal oscillations of the sensor, which are listed on the second row of Table VII. The overall uncertainties for the matching bands are listed on the last row of Table VII.

## VI. DISCUSSION

Unlike other previous studies that used the IR-MAD method to select temporally invariant pixels from the bitemporal image of one sensor, this study employed the IR-MAD method to select PIPs from multispectral images acquired at the same time by two different sensors for intercalibration. Starting from the formula of the intercalibration problem, we demonstrate the reasonableness of employing the IR-MAD technique to select PIPs for intercalibration owing to the linear scale invariance 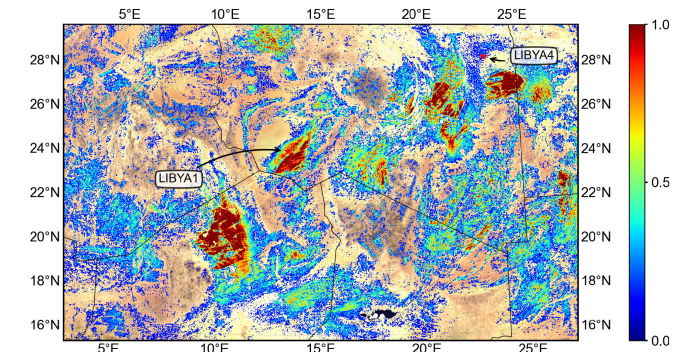property of MAD transformation. The PIPs represent pixels that conform to the potential linear relationship across all matching bands in intercalibration, under the differences caused by a combination of RSR characteristics of the two sensors, the spectral signature of the target, atmospheric conditions, and viewing geometry.

The PIPs are selected statistically from the image pair without a priori knowledge of the target pixel, which is determined based on the existence of a certain underlying linear relationship between the matching bands of the two images. Therefore, different pixels within an image pair, may not conform to this linear relationship due to variations in surface characteristics or differences in atmospheric influence. As a result, the locations of PIPs may vary with different image pairs. It should be noted that when the two images in an image pair are strongly affected by atmospheric conditions or when there is a lack of a sufficient number of samples for statistical analysis due to extensive cloud cover, the number of selected PIPs will decrease, which means it is challenging for IR-MAD to find the underlying linear relationship between the two images. Using these PIPs for regression will result in greater uncertainty. Therefore, such image pairs will be excluded. To examine which areas and surface types are most frequently identified as PIPs, a density map showing the spatial frequency distribution of PIPs of all FY-3B image pairs is depicted in Fig. 13. Similar results can also be obtained with FY-3A.

From Fig. 13, it is evident that PIPs are distributed not only in bright target areas such as deserts but also encompass dark target types like volcanic surfaces. Therefore, intercalibration based on PIPs offers a broader dynamic range. The primary hotspot regions are predominantly located within desert areas, which aligns with our expectations. Deserts exhibit flatter spectral profiles, minimizing the impact of SRF differences between the two sensors. Regarding the spatial distribution pattern of PIPs, our method does not rely on large, spatially uniform regions. Instead, it selects samples at the pixel level, resulting in a higher sample quantity, a richer variety of land surface types, and a broader dynamic range compared to the SNOx method. Furthermore, in addition to internationally recognized PICS such as LIBYA1 and LIBYA4 being found within the distribution area of PIPs, there are several extensive PIPs hotspot regions. These areas hold the potential to serve as valuable calibration sites for future research.

TABLE VII
Uncertainty of the Proposed IR-MAD Method for Intercalibration

| Uncertainty | Source | FY3A VIRR | | | | | FY3B VIRR | | | | |
|---|---|---|---|---|---|---|---|---|---|---|---|
| | | ch1(%) | ch2(%) | ch7(%) | ch8(%) | ch9(%) | ch1(%) | ch2(%) | ch7(%) | ch8(%) | ch9(%) |
| uncertainty for image pair | misregistration atmospheric conditions BRDF effect spectral band differences | 1.46 | 1.30 | 0.69 | 0.68 | 0.65 | 1.50 | 1.23 | 0.85 | 0.78 | 0.89 |
| uncertainty for long-term inter-calibration | polynomial fitting | 1.64 | 2.32 | 1.83 | 0.81 | 1.05 | 1.59 | 2.31 | 1.57 | 1.28 | 0.75 |
| | total error (root sum of squares) | 2.20 | 2.67 | 1.96 | 1.06 | 1.24 | 2.19 | 2.62 | 1.78 | 1.50 | 1.17 |

Another advantage of this method is its ability to implicitly reduce uncertainty. Unlike the SNO-$x$ method, which relies on the spatial uniformity of the surface to select samples, IR-MAD selects samples based on the potential linear relationship between two images. Samples that no longer conform to this linear relationship due to effects such as misregistration, atmospheric disturbances, and BRDF are excluded from the PIPs selection. As a result, the uncertainty introduced by these effects is implicitly minimized during the PIPs selection process of IR-MAD. It's worth noting that this method employs a single SBAF for all PIPs samples, which is a major source of uncertainty in this method. However, as shown in Fig. 13, IR-MAD tends to select targets like deserts that have relatively flat spectral profiles to reduce errors caused by the SRF differences. For long-term intercalibration, variations in atmospheric conditions at different times are the primary source of uncertainty, as evident in Fig. 9. For channels easily affected by atmospheric conditions, their regression slopes exhibit fluctuations and divergence (e.g., channels 1 and 2), while this phenomenon is less pronounced for channels that are less susceptible to atmospheric influence (channels 8 and 9).

This method is not limited to a specific geographical region. We also conducted research in the northwest region of China as our ROI and obtained similar results. Furthermore, this method is not restricted to any particular sensor or satellite platform. It can be applied to SNO and SNO-$x$ events as well. The entire process is generic. The difference lies in the fact that, unlike the two sensors on the same platform in this study, when dealing with sensors on different platforms, additional considerations are required to account for the impact of BRDF effects. Therefore, in such cases, additional constraints should be added to minimize the influence of BRDF. This can be achieved by imposing constraints on the proximity of the two satellite orbits or by using samples from nadir observations for the analysis.

## VII. Concluding Remark

In this study, we propose a novel approach to sensor radiometric intercalibration based on PIPs using the IR-MAD method. Due to the property of linear scale invariance, the IR-MAD method was proposed to statistically select PIPs for intercalibration. The approach requires no prior knowledge of the intercalibration targets. The PIPs do not depend on large spatially homogeneous areas and extend PICS to the pixel-level targets, resulting in a higher sample quantity, a richer variety of land surface types, and a broader dynamic range of reflectance. The PIPs are selected statistically and

can implicitly reduce the uncertainty of intercalibration. This method is generic, not limited to any particular sensor, satellite platform, or geographical region, which is particularly suitable for operational long-term intercalibration.

The implementation of FY-3A&3B VIRR for intercalibration (with the MERSI onboard the same platform as the reference) demonstrates the efficacy of our method. The results show that two widely used PICS for calibration, LIBYA1 and LIBYA4, have been automatically included in the PIPs. Moreover, despite the degradation of the sensors and drift of the satellite orbit over time, the spatial distribution of the PIPs remains consistent. The long-term time series of TOA reflectance over LIBYA1 and LIBYA4 shows that the intercalibrated VIRR is in good agreement with MERSI, with a mean bias of less than 1% and an uncertainty of less than 2% for most channels. For channels with significant seasonal oscillations, the uncertainty is also less than 2.5%. Further exploration of the underlying mechanisms for the seasonal fluctuations in the long-term intercalibration results is still needed. It should be reiterated that although this study used two sensors onboard the same platform for intercalibration, our method is also applicable to other situations where similar sensors for intercalibration are onboard different platforms, such as SNO or SNO-$x$ events.

## Data Availability

The data used in this study are all publicly available in the FY-3A&B satellite archive at FENGYUN Satellite Data Center. These datasets were derived from the public domain resources: http://satellite.nsmc.org.cn/portalsite/default.aspx?currentculture=en-US.

## References

[1] P. N. Slater, S. F. Biggar, J. M. Palmer, and K. J. Thome, "Unified approach to absolute radiometric calibration in the solar-reflective range," *Remote Sens. Environ.*, vol. 77, no. 3, pp. 293–303, Sep. 2001.

[2] P. M. Teillet, J. L. Barker, B. L. Markham, R. R. Irish, G. Fedosejevs, and J. C. Storey, "Radiometric cross-calibration of the Landsat-7 ETM+ and Landsat-5 TM sensors based on tandem data sets," *Remote Sens. Environ.*, vol. 78, nos. 1–2, pp. 39–54, Oct. 2001.

[3] A. K. Heidinger, C. Cao, and J. T. Sullivan, "Using moderate resolution imaging spectrometer (MODIS) to calibrate Advanced Very High Resolution Radiometer reflectance channels," *J. Geophys. Res., Atmos.*, vol. 107, no. D23, pp. 1–12, Dec. 2002.

[4] C. Cao, H. Xu, J. Sullivan, L. Mcmillin, P. Ciren, and Y.-T. Hou, "Intersatellite radiance biases for the high-resolution infrared radiation sounders (HIRS) on board NOAA-15, -16, and -17 from simultaneous nadir observations," *J. Atmos. Ocean. Technol.*, vol. 22, no. 4, pp. 381–395, Apr. 2005.

[5] X. Wu and F. Sun, "Post-launch calibration of GOES imager visible channel using MODIS data," *Proc. SPIE*, vol. 5882, Feb. 2005, Art. no. 58820N.

[6] A. Wu, C. Cao, and X. Xiong, "Using MODIS to track calibration stability of the AVHRR on NOAA 15–18," *Proc. SPIE*, vol. 6298, Oct. 1117, Art. no. 629812.

[7] A. K. Heidinger, W. C. Straka, C. C. Molling, J. T. Sullivan, and X. Wu, "Deriving an inter-sensor consistent calibration for the AVHRR solar reflectance data record," *Int. J. Remote Sens.*, vol. 31, no. 24, pp. 6493–6517, Dec. 2010.

[8] S. Uprety, C. Cao, X. Xiong, S. Blonski, A. Wu, and X. Shao, "Radiometric intercomparison between suomi-NPP VIIRS and Aqua MODIS reflective solar bands using simultaneous nadir overpass in the low latitudes," *J. Atmos. Ocean. Technol.*, vol. 30, no. 12, pp. 2720–2736, Dec. 2013.

[9] P. M. Teillet, P. N. Slater, Y. Ding, R. P. Santer, R. D. Jackson, and M. S. Moran, "Three methods for the absolute calibration of the NOAA AVHRR sensors in-flight," *Remote Sens. Environ.*, vol. 31, no. 2, pp. 105–120, Feb. 1990.

[10] P. N. Slater, S. F. Biggar, K. J. Thome, D. I. Gellman, and P. R. Spyak, "Vicarious radiometric calibrations of EOS sensors," *J. Atmos. Ocean. Technol.*, vol. 13, no. 2, pp. 349–359, Apr. 1996.

[11] P. M. Teillet et al., "A generalized approach to the vicarious calibration of multiple Earth observation sensors using hyperspectral data," *Remote Sens. Environ.*, vol. 77, no. 3, pp. 304–327, Sep. 2001.

[12] K. J. Thome, "Absolute radiometric calibration of Landsat 7 ETM+ using the reflectance-based method," *Remote Sens. Environ.*, vol. 78, nos. 1–2, pp. 27–38, Oct. 2001.

[13] C. J. Bruegge et al., "Early validation of the Multi-Angle Imaging SpectroRadiometer (MISR) radiometric scale," *IEEE Trans. Geosci. Remote Sens.*, vol. 40, no. 7, pp. 1477–1492, Jul. 2002.

[14] K. J. Thome, D. L. Helder, D. Aaron, and J. D. Dewald, "Landsat-5 TM and Landsat-7 ETM+ absolute radiometric calibration using the reflectance-based method," *IEEE Trans. Geosci. Remote Sens.*, vol. 42, no. 12, pp. 2777–2785, Dec. 2004.

[15] H. Cosnefroy, M. Leroy, and X. Briottet, "Selection and characterization of Saharan and Arabian desert sites for the calibration of optical satellite sensors," *Remote Sens. Environ.*, vol. 58, no. 1, pp. 101–114, Oct. 1996.

[16] X. Xiong, "Using the Sonoran and Libyan desert test sites to monitor the temporal stability of reflective solar bands for Landsat 7 Enhanced Thematic Mapper Plus and Terra Moderate Resolution Imaging Spectroradiometer sensors," *J. Appl. Remote Sens.*, vol. 4, no. 1, Apr. 2010, Art. no. 043525.

[17] G. Chander, X. Xiong, T. Choi, and A. Angal, "Monitoring on-orbit calibration stability of the Terra MODIS and Landsat 7 ETM+ sensors using pseudo-invariant test sites," *Remote Sens. Environ.*, vol. 114, no. 4, pp. 925–939, Apr. 2010.

[18] P. Minnis, D. R. Doelling, L. Nguyen, W. F. Miller, and V. Chakrapani, "Assessment of the visible channel calibrations of the VIRS on TRMM and MODIS on Aqua and Terra," *J. Atmos. Ocean. Technol.*, vol. 25, no. 3, pp. 385–400, Mar. 2008.

[19] Y. J. Kaufman and B. N. Holben, "Calibration of the AVHRR visible and near-IR bands by atmospheric scattering, ocean glint and desert reflection," *Int. J. Remote Sens.*, vol. 14, no. 1, pp. 21–52, Jan. 1993.

[20] O. Hagolle, J.-M. Nicolas, B. Fougnie, F. Cabot, and P. Henry, "Absolute calibration of VEGETATION derived from an interband method based on the sun glint over ocean," *IEEE Trans. Geosci. Remote Sens.*, vol. 42, no. 7, pp. 1472–1481, Jul. 2004.

[21] X. Xiong, J. Sun, and W. Barnes, "Intercomparison of on-orbit calibration consistency between Terra and Aqua MODIS reflective solar bands using the moon," *IEEE Geosci. Remote Sens. Lett.*, vol. 5, no. 4, pp. 778–782, Oct. 2008.

[22] T. C. Stone, W. B. Rossow, J. Ferrier, and L. M. Hinkelman, "Evaluation of ISCCP multisatellite radiance calibration for geostationary imager visible channels using the moon," *IEEE Trans. Geosci. Remote Sens.*, vol. 51, no. 3, pp. 1255–1266, Mar. 2013.

[23] C. Cao and A. K. Heidinger, "Intercomparison of the longwave infrared channels of MODIS and AVHRR/NOAA-16 using simultaneous nadir observations at orbit intersections," *Proc. SPIE*, vol. 4814, pp. 306–316, Sep. 2002.

[24] C. Cao, X. Xiong, A. Wu, and X. Wu, "Assessing the consistency of AVHRR and MODIS L1B reflectance for generating fundamental climate data records," *J. Geophys. Res., Atmos.*, vol. 113, no. D9, May 2008, doi: 10.1029/2007JD009363.

[25] C. H. Dong et al., "An overview of a new Chinese weather satellite FY-3A," *Bull. Amer. Meteorol. Soc.*, vol. 90, no. 10, pp. 1531–1544, 2009.

[26] L. Sun et al., "On-orbit response variation analysis of FY-3 mersi reflective solar bands based on Dunhuang site calibration," *Spectrosc. Spectral Anal.*, vol. 32, no. 7, pp. 1869–1877, 2012.

[27] X. Hu et al., "Calibration for the solar reflective bands of medium resolution spectral imager onboard FY-3A," *IEEE Trans. Geosci. Remote Sens.*, vol. 50, no. 12, pp. 4915–4928, Dec. 2012.

[28] J. Wang, X. Hu, Y. He, and K. Gao, "Response degradation analysis of Fengyun-3A medium-resolution spectral imager based on intelligent detection of invariant pixels," *Acta Optica Sinica*, vol. 39, no. 9, 2019, Art. no. 0912001.

[29] G. Chander, B. L. Markham, and D. L. Helder, "Summary of current radiometric calibration coefficients for Landsat MSS, TM, ETM+, and EO-1 ALI sensors," *Remote Sens. Environ.*, vol. 113, no. 5, pp. 893–903, May 2009.

[30] G. Thuillier et al., "The solar spectral irradiance from 200 to 2400 nm as measured by the SOLSPEC spectrometer from the ATLAS and EURECA missions," *Sol. Phys.*, vol. 214, pp. 1–22, May 2003.

[31] G. Chander et al., "Applications of spectral band adjustment factors (SBAF) for cross-calibration," *IEEE Trans. Geosci. Remote Sens.*, vol. 51, no. 3, pp. 1267–1281, Mar. 2013.

[32] A. A. Nielsen, K. Conradsen, and J. J. Simpson, "Multivariate alteration detection (MAD) and MAF postprocessing in multispectral, bitemporal image data: New approaches to change detection studies," *Remote Sens. Environ.*, vol. 64, no. 1, pp. 1–19, 1998.

[33] M. J. Canty, A. A. Nielsen, and M. Schmidt, "Automatic radiometric normalization of multitemporal satellite imagery," *Remote Sens. Environ.*, vol. 91, nos. 3–4, pp. 441–451, Jun. 2004.

[34] M. Schmidt, E. A. King, and T. R. McVicar, "A method for operational calibration of AVHRR reflective time series data," *Remote Sens. Environ.*, vol. 112, no. 3, pp. 1117–1129, Mar. 2008.

[35] A. A. Nielsen, "The regularized iteratively reweighted mad method for change detection in multi-and hyperspectral data," *IEEE Trans. Image Process.*, vol. 16, no. 2, pp. 463–478, Feb. 2007.

[36] M. J. Canty and A. A. Nielsen, "Automatic radiometric normalization of multitemporal satellite imagery with the iteratively re-weighted MAD transformation," *Remote Sens. Environ.*, vol. 112, no. 3, pp. 1025–1036, Mar. 2008.

[37] X. Hu et al., "Preliminary selection and characterization of pseudo-invariant calibration sites in Northwest China," *Remote Sens.*, vol. 12, no. 16, p. 2517, Aug. 2020.

[38] H. Hotelling, "Relations between two sets of variates," in *Breakthroughs in Statistics*. Berlin, Germany: Springer, 1992, pp. 162–190.

[39] L. Wang, X. Hu, L. Chen, and L. He, "Consistent calibration of VIRR reflective solar channels onboard FY-3A, FY-3B, and FY-3C using a multisite calibration method," *Remote Sens.*, vol. 10, no. 9, p. 1336, Aug. 2018. [Online]. Available: https://www.mdpi.com/2072-4292/10/9/1336

[40] L. Sun, H. Qiu, R. Wu, J. Wang, L. Zhang, and P. Zhang, "Long-term consistent recalibration of VIRR solar reflectance data record for fengyun polar-orbiting satellites," *J. Meteorolog. Res.*, vol. 35, no. 6, pp. 926–942, Dec. 2021.

**Junwei Wang** received the B.Eng. degree in optoelectronics information science and engineering from the Beijing Institute of Technology, Beijing, China, in 2018, where he is currently pursuing the Ph.D. degree in optical engineering with the School of Optoelectronics.

His research interests include sensor calibration and remote sensing applications.

**Xiuqing (Scott) Hu** (Member, IEEE) received the B.S. degree in atmospheric science from Nanjing University, Nanjing, China, in 1996, the M.S. degree in cartography and geographical information system from Beijing Normal University, Beijing, China, in 2004, and the Ph.D. degree in quantitative remote sensing science from the Institute of Remote Sensing Applications, Chinese Academy of Sciences, Beijing, in 2012.

He has been a professor of engineering since 2010. He is currently the Chief Engineer of the ground segment system for Fengyun-3 polar-orbiting satellites and the Group Leader of satellite calibration/validation of the National Satellite Meteorological Center, China Meteorological Administration (NSMC/CMA), Beijing. His research interests include high-level framework design and requirement reviewing of the Chinese Third Generation Meteorological Satellite Constellation; calibration theory and technology of satellite remote sensors, research on remote sensing data preprocessing and quality improvement technology; and research on remote sensing inversion scientific algorithm and remote sensing big data application.

Dr. Hu was the previous Chair and is now the Vice Chair of the GSICS Research Working Group (GRWG) under WMO and CGMS.



**Kun Gao** (Member, IEEE) received the B.E. degree in electrical engineering and the Ph.D. degree in instrument science and engineering from Zhejiang University, Hangzhou, China, in 1995 and 2002, respectively.

From 2002 to 2004, he was a Post-Doctoral Fellow with Tsinghua University, Beijing, China. Since 2005, he has been with the Beijing Institute of Technology, Beijing, working on infrared technology and real-time image processing.

Dr. Gao is a member of the Optical Society of China.



**Yuqing He** received the B.S. degree in physical electronics and the Ph.D. degree in optical engineering from the Beijing Institute of Technology, Beijing, China, in 1998 and 2003, respectively.

She is currently an Associate Professor with the School of Optics and Photonics, Beijing Institute of Technology. Her research interests include photoelectronic imaging, sensor radiometric calibration, and intelligent image analysis.



**Ling Wang** received the Ph.D. degree in cartography and geographic information systems from Nanjing University, Nanjing, China, in June 2013.

She is currently an Associate Researcher with the National Satellite Meteorological Center (NSMC), Beijing, China. Her research interests include radiometric calibration of solar bands of meteorological satellite sensors.



**Guorong Li** received the B.S. degree in optoelectronics information science and engineering and the M.S. degree in optical engineering from the Beijing Institute of Technology, Beijing, China, in 2019 and 2022, respectively.

His research interests include remote sensing image processing and cross-calibration of optical remote sensors.



**Na Xu** received the B.S. degree in atmospheric science from the Ocean University of China, Qingdao, China, in 2005, and the Ph.D. degree in atmospheric physics and environment from the Institute of Atmospheric Physics, Chinese Academy of Sciences, Beijing, China, in 2010.

She was the Chief Designer of the product generation system (PGS) of Fengyun Geostationary and polar orbiting series satellites and the instrument responsible for the Fengyun-3 medium resolution spectral imager. She is currently the Director of the Research and Development Division of FengYun Satellite Program, National Satellite Meteorological Center, China Meteorological Administration, Beijing. She is also the Deputy Chief Engineer of Fengyun-3 composite star and also the Chief Director of PGS for FengYun-3 and FengYun-4 Projects. She has long been engaged in research related to quantitative remote sensing of Fengyun meteorological satellites and has done a lot of work in the calibration of remote sensing instruments and inversion of geophysical parameters, making outstanding contributions to promoting the improvement of remote sensing instrument process of Fengyun meteorological satellites, and the improvement of observation data quality and application capability of Fengyun optical remote sensors.

Dr. Xu is a member of the Global Space-Based Intercalibration System (GSICS/WMO). She is the Co-Chair of CGMS WG II.



**Peng Zhang** (Senior Member, IEEE) was born in Shaanxi, China, in October 1970. He received the Ph.D. degree in atmospheric physics from the Institute of Atmospheric Physics, Chinese Academy of Sciences (IAP/CAS), Beijing, China, in 1998.

He has been the Director-General of the CMA Meteorological Observation Centre (MOC) since 2023. He has been the Chief Director of the Chinese FengYun-3 (FY-3) Polar-Orbiting Meteorological Satellite Program since 2014 and is intensively involved in conceiving, developing, and operating the FY-3 satellite ground segment. He has authored or coauthored over 200 papers published in refereed scientific journals to date. His research interests include atmospheric remote sensing, satellite calibration and validation, and atmospheric radiative transfer calculation.